MERCI: Mixed Curvature-Based Elements for Computing Equilibria of Thin Elastic Ribbons

RAPHAËL CHARRONDIÈRE, Inria Research Centre of Université Grenoble Alpes, Montbonnot Saint-Martin, France and Laboratoire Jean Kuntzmann (UMR 5224), Grenoble, France
SÉBASTIEN NEUKIRCH, Institut Jean le Rond d'Alembert, Sorbonne Université, Paris, France and CNRS (UMR 7190), Paris, France
FLORENCE BERTAILS-DESCOUBES, Inria Research Centre of Université Grenoble Alpes, Montbonnot-Saint-Martin, France and Laboratoire Jean Kuntzmann (UMR 5224), Grenoble, France

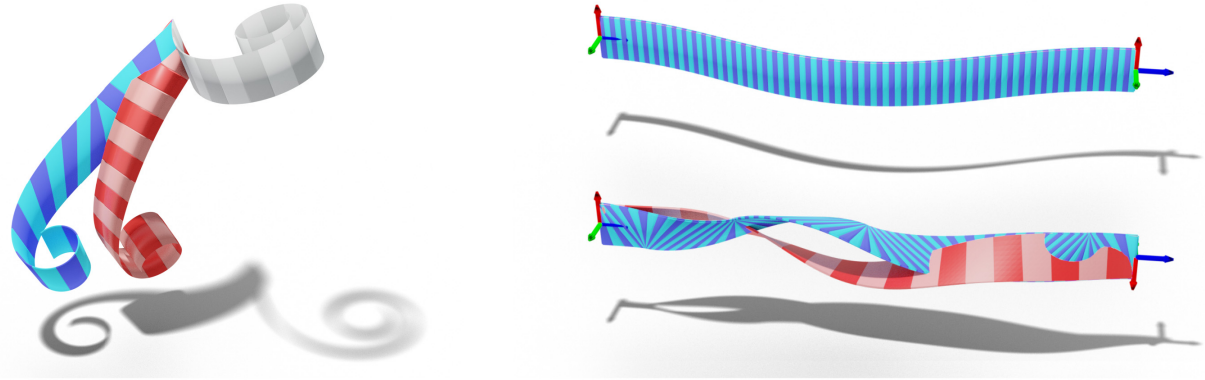

Fig. 1. A Wunderlich thin elastic ribbon (in blue, computed with our MERCI code) does not deform like a rectangular Kirchhoff thin elastic rod (in red, computed (left) as a flat super-clothoid, and (right) with a shooting technique). Left: Starting from the exact same curly natural shape (in gray), the configuration of the ribbon under its own weight substantially diverges from that of the rod even though both have the same rectangular cross-section and the same clamping orientation. Right: Noticeable differences also appear in a clamped-clamped scenario where the ribbon/rod (with $w/L = 1/12$) is twisted by a half-turn (from top to bottom). In these two scenarios, while the centreline of the rod remains inextensible, its *surface* stretches too much to represent a ribbon correctly. Note that as the ribbon and the rod possess two distinct equilibria in both scenarios, we make sure to have them buckle "on the same side" to be able to compare their geometry in a meaningful way.

Thin elastic ribbons represent a class of intermediary objects lying in-between thin elastic plates and thin elastic rods. Although the two latter families of thin structures have received much interest from the Computer Graphics community over the last decades, ribbons have seldom been considered and modelled numerically so far, in spite of a growing number of applications in Computer Design.

In this article, starting from the reduced developable ribbon models [Sadowsky 1929; Wunderlich 1962] recently popularised in Soft Matter Physics, we propose a both accurate and efficient algorithm for computing the statics of thin elastic ribbons. Inspired by the super-clothoid model for thin elastic rods, our method relies on compact ribbon elements whose normal curvature varies linearly with respect to arc length s, while their geodesic torsion is quadratic in s. In contrast, however, for the sake of efficiency, our algorithm avoids building a fully reduced kinematic chain and instead treats each element independently, gluing them only at the final solving stage through well-chosen bilateral constraints.

Thanks to this mixed variational strategy, which yields a banded Hessian, our algorithm recovers the linear complexity of low-order models while preserving the high-order convergence of curvature-based models. As a result, our approach is scalable to a large number of elements, and suitable for various boundary conditions and unilateral contact constraints, making it possible to handle challenging scenarios such as confined buckling experiments or Möbius bands with contact. Remarkably, our mixed algorithm proves an order of magnitude faster compared to Discrete Elastic Ribbon models of the literature while achieving, in a few seconds only, high accuracy levels that remain out of reach for such low-order models. Additionally, our numerical model can incorporate various ribbon energies, including the RIBEXT model for quasi-developable ribbons recently introduced in Physics [Audoly and Neukirch 2021], which allows to transition smoothly between a rectangular Kirchhoff rod and a (developable) Sadowsky ribbon. Our numerical scheme is carefully

Authors' Contact Information: Raphaël Charrondière, Inria Research Centre of Université Grenoble Alpes, Montbonnot Saint-Martin, Auvergne-Rhône-Alpes, France and Laboratoire Jean Kuntzmann (UMR 5224), Grenoble, Auvergne-Rhône-Alpes, France; e-mail: raphael.charrondiere@inria.fr; Sébastien Neukirch, Institut Jean le Rond d'Alembert, Sorbonne Université, Paris, Île-de-France, France and CNRS (UMR 7190), Paris, Île-de-France, France; e-mail: sebastien.neukirch@upmc.fr; Florence Bertails-Descoubes, Inria Research Centre of Université Grenoble Alpes, Montbonnot-Saint-Martin, Auvergne-Rhône-Alpes, France and Laboratoire Jean Kuntzmann (UMR 5224), Grenoble, Auvergne-Rhône-Alpes, France; e-mail: Florence.Descoubes@inria.fr.

This work is licensed under a Creative Commons Attribution-NoDerivs International 4.0 License.

© 2024 Copyright held by the owner/author(s).
ACM 0730-0301/2024/08-ART160
https://doi.org/10.1145/3674502

validated against demanding experiments of the Physics literature, which demonstrates its accuracy, efficiency, robustness, and versatility.

Our Merci code is publicly available at https://gitlab.inria.fr/elan-public-code/merci for the sake of reproducibility and future benchmarking.

CCS Concepts: • **Computing methodologies** → **Animation**; **Physical simulation;**

Additional Key Words and Phrases: Thin elastic ribbon, curvature-based element, constraints, contact, möbius band

ACM Reference Format:
Raphaël Charrondière, Sébastien Neukirch, and Florence Bertails-Descoubes. 2024. MERCI: Mixed Curvature-Based Elements for Computing Equilibria of Thin Elastic Ribbons. *ACM Trans. Graph.* 43, 5, Article 160 (August 2024), 26 pages. https://doi.org/10.1145/3674502

1 Introduction

Thin elastic ribbons form a large class of structures encompassing natural and manufactured objects that can be observed at various scales, from macromolecules and carbon nanoribbons at the nanoscale to plant leaves, paper strips, and wooden slats at the macroscopic scale.

A thin (rectangular) ribbon is formally defined as a thin structure with a thickness h negligible compared to its width w, the latter being itself negligible compared to its length L. This leads to an object with three characteristic dimensions h, w, and L, satisfying $h \ll w \ll L$ (see Figure 2). As such, a thin ribbon can be considered to be an intermediary object lying in-between a thin plate (for which $h \ll w \sim L$) and a thin rod (for which $h \sim w \ll L$).

The peculiar, narrow geometry of ribbons has led physicists to imagine *reduced* models for ribbons, where all kinematic and elastic quantities are, similarly to rod models, concentrated on a mid-line called the centreline (see Figure 3). However, a crucial difference between ribbons and rods is that the surface of a ribbon is, like the surface of a plate, hardly stretchable. The first reduced models of ribbons, namely the Sadowsky [1929] and Wunderlich [1962] models, even consider the ribbon surface to be perfectly inextensible, i.e., isometric to the initial flat rectangle, and hence developable. While the Sadowsky model is limited to narrow ribbons (small w), the Wunderlich model captures singularities occurring near the boundaries, and as such extends the validity domain to ribbons of finite width w. Recently, a quasi-inextensible ribbon model [Audoly and Neukirch 2021; Sano and Wada 2018] was introduced to better account for the little stretching appearing especially in narrow ribbons, allowing for a smooth transition between Kirchhoff rods and Sadowsky ribbons.

In Computer Graphics, such reduced ribbon models remain mostly unknown. Yet, recent years have seen the emergence of a large number of virtual design applications involving static equilibria of thin elastic ribbons, from 3D free-form weaving [Ren et al. 2021; Vekhter et al. 2019] to the design of new flexible metamaterials [Signer et al. 2021] and programmable matter [Hafner and Bickel 2021; Jourdan et al. 2022]. For these applications, it is desirable to compute equilibrium shapes and forces with a high level of accuracy, suitable for the design of real objects, while restraining the inherent computational cost. This calls for a *minimalist yet predictive* static ribbon simulator, able to cope with various constraints such as clamping conditions and contact.

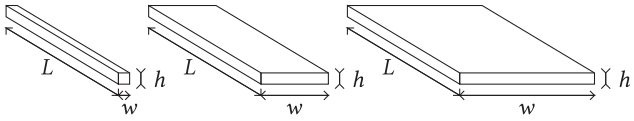

Fig. 2. Schematic of a thin rectangular ribbon (middle), lying in-between a thin rod (left) and a thin plate (right).

In this article, we introduce a static simulator dedicated to thin elastic ribbons. Our numerical scheme is well-suited for the latest reduced physical models elaborated for ribbons, which are still the topic of active investigations in physics. Our approach, based on compact curvature-based elements, is able to resolve challenging scenarios involving clamped-clamped boundary conditions and contacting constraints in a both accurate and efficient way, often outperforming the capabilities of the few existing implementations of reduced ribbon models made in Physics, and at the same time offering a fast and reliable tool suitable for virtual prototyping in Computer Graphics.

2 Related Work

In Computer Graphics, a large body of work has been conducted since the 1990's for simulating thin elastic bodies, especially thin elastic rods, plates and shells. With the increasing interest of the community for prototyping ribbons, it is interesting to note that some of these numerical models are now being directed towards the simulation of ribbons—at the risk of yielding an incorrect physical behaviour or an unnecessarily high cost.

Ribbons as rods or plates. Motivated by applications in hair and cloth animation, the Computer Graphics community has focused in the past on computing the statics and dynamics of thin elastic rods [Bergou et al. 2010, 2008; Bertails et al. 2006; Casati and Bertails-Descoubes 2013; Hadap 2006; Pai 2002; Spillmann and Teschner 2007] and plates [Baraff and Witkin 1998; Choi and Ko 2002; English and Bridson 2008; Narain et al. 2012]. In particular, for visual purposes rod models have sometimes been extrapolated to emulate the behaviour of narrow ribbons [Bergou et al. 2008, Fig. 5] [Casati and Bertails-Descoubes 2013, Fig. 1, 12], without verifying the validity of the rod model in this extended case.

More critically, all the recent virtual design applications mentioned in the introduction, which require a high level of predictability, have been developed by simulating ribbons either as a flat rectangular rod, using a thin elastic rod simulator [Hafner and Bickel 2021; Ren et al. 2021], or as a strip of an elastic plate, based on a thin plate simulator [Bartels and Hornung 2015; Huang et al. 2020; Signer et al. 2021]. While the former class of models cannot represent ribbons accurately as soon as they deform in 3D (in particular, the quasi-developability of the ribbon surface fails to be preserved when torsion is at play, see Figure 1), the latter may be unnecessarily costly as it strives to capture transverse deformations (solving for equations across the width) which can be neglected in ribbons. Additionally, approaching the inextensible limit of a ribbon (i.e., with a vanishing thickness h) turns out to be particularly challenging using a plate model. Indeed, plate models usually suffer from a degraded convergence

as they are made thinner and thinner ($h \to 0$), a phenomenon called *locking* [Arnold and Brezzi 1997]. As explained below, the Computer Graphics community has spent many years striving to simulate inextensible plates, and fighting against locking.

Simulation of quasi-inextensible surfaces. To bypass the difficulty of handling quasi-inextensible—hence stiff—plates, the first cloth simulators developed in Graphics used to rely on an excessively low stiffness (disregarding the apparent thickness of the plate), causing unrealistic, overly stretchy deformations [Carignan et al. 1992; Terzopoulos et al. 1987]. Implicit integration helped resolve stiff systems in a stable way while using large time steps [Baraff and Witkin 1998], however at the price of introducing some artificial numerical damping, and requiring a large number of iterations to converge in the limit of inextensible cloth. To solve these issues, various works have attempted in the last decades to build efficient solvers for quasi-inextensible cloth. Techniques range from the introduction of new integration schemes [Choi and Ko 2002; Hauth et al. 2003] to the combination of an overly soft plate material with some strain limiting technique [Goldenthal et al. 2007; Provot 1995; Thomaszewski et al. 2009], or even the use of non-conforming inextensible mesh elements [English and Bridson 2008]. To our knowledge, all these works focus on a triangular or quad mesh to represent the cloth surface, and none of them leverages a reduced parametrisation dedicated to an inextensible surface. The bending energy[1] of the cloth is classically discretised using an edge-based discrete formula for the mean curvature [Bridson et al. 2003; Chen et al. 2018; Grinspun et al. 2003; Solomon et al. 2012]. However such discrete schemes have been shown to converge slowly, if at all, when the plate undergoes singularities, like for instance in the lateral bending test [Romero et al. 2021] where a boundary layer emerges near the clamping. In their origami-like representation of developable surfaces, in which fold lines are explicitly provided by a user, Solomon et al. [2012, Section 5.1] sidestep the problem by discarding singular areas in the bending energy computation of the smooth patches.

Interestingly, Schreck et al. [2015] combine standard cloth simulation [Narain et al. 2012] with an explicit developable surface representation to simulate paper crumpling. At each time step, a coarse simulation is performed and the resulting surface is remeshed using elementary developable surfaces such as planar patches or generalised cones emerging from singular locations that are detected on the fly. Still, similarly to most former works, the developability constraint is enforced as a post-processing step on top of an overly stretchy step. In contrast, although our approach is for now limited to narrow plates (singularities may only happen at the boundaries), we directly formulate the discrete equations for a perfectly developable plate—possibly relaxed to a quasi-developable plate—and capture smooth deformations as well as singularities using a unique surface representation.

Computer-aided design of developable surfaces. Originally, developable surfaces, i.e. surfaces isometric to a plane [Do Carmo 2016], found some practical importance to the sheet-metal-based industry, where flat patches are deformed without in-plane distortion – or, in other words, by pure bending – before being assembled. In this context, a number of algorithms were proposed in Computer-Aided Design from the 80's in order to manipulate developable patches virtually [Pottmann and Farin 1995]. Recently, there has been renewed interest for developable surfaces in Computer Graphics, owing to the emergence of new applications for virtual prototyping, such as architectural design from bent panels [Kilian et al. 2008], pattern-based cloth modelling [Decaudin et al. 2006; Pietroni et al. 2022], or paper-based object manipulation and origami art [Bös et al. 2017; Dudte et al. 2016; Signer et al. 2021; Tang et al. 2016; Wolf et al. 2021]. In this context, a range of different characterisations of developable surfaces were explored in the continuous and discrete settings, from ruled surfaces to envelopes of tangent planes and rank deficient second fundamental forms [Bo and Wang 2007; Inza et al. 2023; Liu et al. 2006; Pan et al. 2016; Tang et al. 2016]. Interestingly, new reduced parametrisations were even proposed in the latest years, in particular networks of orthogonal geodesics [Rabinovich et al. 2018a, b]. However, to our knowledge such kinematic descriptions are not associated to any physically realistic elastic energy for the deformed surface: an ad-hoc discrete surface energy, such as the Laplacian energy of the displacement w.r.t the rest shape, is generally used. The accurate computation of the mean curvature of the surface, which is a difficult task especially in the presence of singularities (e.g. when the rulings cross each other at the boundary), is then omitted.

As such, our work can be seen as orthogonal to these geometrical methods. We do not search for the best geometric parametrisation to manipulate flat surfaces isometrically, but focus instead on accurately solving the physics of ribbons in the presence of singularities. This objective raises a number of specific numerical difficulties, hardly overcome in the past. Our choice of degrees of freedom takes inspiration from the curvature-based discretisation of Kirchhoff rods [Casati and Bertails-Descoubes 2013; Charrondière et al. 2020], coupled with the explicit representation of rulings over the developable surface of the ribbon. The developability assumption can be slightly relaxed so as to extend the range of physical validity of our simulator, as shown in the last part of the article.

Overall, our work can be seen as a first step in Computer Graphics towards the merging of developable surface parametrisation and quasi-inextensible plate simulation. One key element of our approach is to rely upon reduced (1D) physical models for modelling quasi-inextensible plates, which so far have been successfully developed in Physics in the specific case of narrow plates: *reduced ribbon models*.

Simulation of reduced ribbon models. The equations of reduced ribbon models, extensively described in Section 4, have been so far mostly solved by physicists using shooting techniques, i.e. taking the strong form of the equations with boundary conditions and solving them with a Newton solver [Moore and Healey 2019; Neukirch and Audoly 2021; Starostin and van der Heijden 2015]. Although this kind of technique is powerful enough to compute accurate phase diagrams by continuation, its success remains highly dependent on the choice of the first iterate—the warm start—and requires tiny parameter changes to go from one static configuration to another. Beyond the tedious setup procedure it involves, shooting remains difficult to extend to intermittent

[1] The bending energy of a developable plate reads $\iint H^2 d\mathcal{A}$, where H is the mean curvature of the surface [Sadowsky 1929] [Audoly and Pomeau 2010, Section 6.6].

boundary conditions like contact. In the absence of flexible and publicly available numerical tools for simulating ribbons subject to contact and clamping conditions, researchers in Mechanics still rely, like in Computer Graphics, on thin elastic rod simulators for applications in design, even though structures of interest are ribbons [Lestringant and Kochmann 2020].

Very recently, two interesting alternatives were inspired by rod models developed in Computer Graphics. On the one hand, the Discrete Elastic Rod (DER) model [Bergou et al. 2010, 2008] has been extended to Wunderlich ribbons in the naturally flat case, first in Computer Graphics [Shen et al. 2015], then in Mechanics [Huang et al. 2022; Korner et al. 2021], and validated against the Möbius band experiment. Huang et al. [2022] even incorporates the quasi-developable RibExt energy [Audoly and Neukirch 2021] to the DER formulation, and replicate some of the numerical experiments performed initially by Audoly and Neukirch [2021]. As shown in our article (see Section 7.4), one important drawback of DER ribbons is the low order (segment-based) geometry of the underlying model, which calls for a very high number of segments—hence some significant computational cost—to reach accurate configurations. In addition, various regularisation strategies may be required to reach a given equilibrium, especially for dealing with singular points or large ribbons.

On the other hand, Charrondière et al. [2020] have instead explored a high order strategy, by developing curvature-based elements for inextensible ribbons. The key of their numerical approach is to adapt the adaptive power series computation introduced in the super-clothoid model [Casati and Bertails-Descoubes 2013] to the accurate, quasi-formal computation of all kinematic terms of Sadowsky and Wunderlich ribbons. While this approach is capable of computing accurate equilibria for clamped-free inextensible ribbons, possibly with natural curvature, it is not well-suited for clamped-clamped conditions nor to a very large number of elements – often necessary to deal with contact –, owing to its chained kinematic structure.

3 Contributions

In this article, we develop a realistic yet efficient static simulator dedicated to thin elastic ribbons subject to various constraints, with a high level of predictability adapted to the needs of virtual prototyping. Our work builds upon the accurate model of Charrondière et al. [2020] based on a curvature-based discretisation of both the Sadowsky [1929] and the Wunderlich [1962] reduced models for thin developable ribbons. After describing the reduced physical ribbon model of the literature (Section 4), we substantially improve [Charrondière et al. 2020]'s numerical model and validate it by:

- Making it scalable to a large number of elements, thanks to a mixed algorithm gluing curvature-based elements together through well-chosen bilateral constraints. Our approach, which decreases the complexity from cubic to linear, is able to tackle complex scenarios involving various boundary conditions and contact (Section 5);
- Extensively verifying the numerical accuracy of our mixed algorithm against quantitative 2D and 3D scenarios, with and without contact (Sections 6, 7 and 8);
- Comparing thoroughly our mixed curvature-based formulation, in terms of accuracy and cost, against a recent static DER-like implementation of reduced ribbons [Korner et al. 2021]. Because it combines the advantages of both high-order convergence and linear complexity, our mixed algorithm is found to offer a remarkably effective alternative to DER, showing on our tests more than 100× speed-ups for low to moderate accuracy, and unique capabilities to reach high accuracies (Section 7.4);
- Incorporating a new ribbon energy for an extended validity range of our approach, namely the recent RibExt energy for quasi-developable ribbons [Audoly and Neukirch 2021], which allows to transition smoothly between a rectangular-section Kirchhoff rod and a (developable) Sadowsky ribbon (Section 9).

4 Geometry and Physics of Ribbons

Elastic rods, Figure 2 left, have a small cross-section and consequently all geometric quantities are defined on a 1D model, with centreline $\mathbf{r}(s)$. Their equilibrium equations are ordinary differential equations, where the arc length s is the only independent variable. Elastic plates (or shells), Figure 2 right, have a small thickness but comparable width and length. Consequently, the description of their geometry involves 2 independent variables (e.g., x and y in the linear case) and the equilibrium equations controlling their displacement ($z = z(x, y)$ in the linear case) are partial differential equations. In both theories, the thickness of the rod or the plate is small and hence their stretching rigidity (which scales as $O(h)$) is large compared with their bending rigidity (which scales as $O(h^3)$). As a consequence, little stretching is present in equilibrium configurations [Audoly and Pomeau 2010; Dill 1992].

Elastic ribbons, Figure 2 middle, are intermediate structures between rods and plates. As their width is small compared with their length, the mechanical state from the plate description is averaged over the width to obtain a 1D model. Consequently, as for rods, ribbons have equilibrium equations which involve a centreline $\mathbf{r}(s)$ and which are ordinary differential equations. Nevertheless, their large width-to-thickness ratio makes their behaviour clearly distinct from that of elastic rods, see Figure 1.

In rods models, the large stretching rigidity often leads to dealing with an inextensible centreline, $|\mathbf{r}'(s)| = 1$, but the material of the cross-section around the centreline is considered extensible (and incidentally this is how the bending rigidity of rods is computed).

For ribbons, the large stretching rigidity has motivated early models [Hinz and Fried 2015; Sadowsky 1929; Todres 2015; Wunderlich 1962] to consider an inextensible mid-surface. Such reduced parameterisations involve an inextensible centreline $\mathbf{r}(s)$ and a set of rulings to geometrically describe the (inextensible) mid-surface of the ribbon. A more recent ribbon model keeps the inextensibility of the centreline ($|\mathbf{r}'(s)| = 1$) but allows for stretching of the mid-surface [Audoly and Neukirch 2021], and we show in Section 9 that this finite (although large) stretching resistance may in some cases have a large impact on the behaviour of the ribbon.

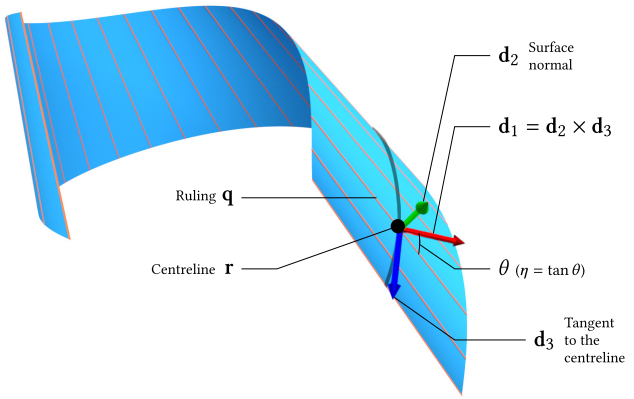

Fig. 3. Kinematics of a developable ribbon.

In the following, we restrict ourselves to the case of a rectangular ribbon with a uniform thickness h, and we denote w the width and L the length of the ribbon (see Figure 2, middle). We consider the rest mid-surface to be flat or possibly curved in the normal direction (see Figure 1, left). For the sake of simplicity, we only consider rest mid-surfaces with no geodesic curvature, i.e. the surface can only bend around its tangent axes $\mathbf{d}_1$ and $\mathbf{d}_3$ (through *normal curvature* and *geodesic torsion*, respectively), but not around its normal $\mathbf{d}_2$ (see Figure 3). We leave this extension [Dias and Audoly 2014; Yu et al. 2021] for future work. As the geodesic curvature is conserved when the ribbon deforms, geodesic curvature stays zero at all times.

4.1 Developable Case

We start with the case of a purely inextensible ribbon, that is a ribbon whose mid-surface can only deform isometrically. As the rest mid-surface is rectangular with no Gaussian curvature, it means that the ribbon mid-surface always preserves a vanishing Gauss curvature, hence it is *developable*.

Kinematics. The developability of the ribbon mid-surface allows one to describe its shape with only two scalar functions, the *normal curvature* $\kappa(s)$, and the *ruling direction* $\eta(s)$. These two quantities are described hereafter.

As illustrated in Figure 3, the variable $s \in [0, L]$ is the arc length along the centreline $\mathbf{r}(s)$, which is a 3D curve along the ribbon. To follow the deformation of the material around the centreline, we use a set of three orthonormal Cosserat directors $\mathcal{R} = \{\mathbf{d}_1, \mathbf{d}_2, \mathbf{d}_3\}$ which are organised as columns inside the matrix $\mathcal{R}(s)$.

This material frame is such that $\mathbf{d}_2$ is normal to the ribbon surface and $\{\mathbf{d}_1, \mathbf{d}_3\}$ span the tangent plane to the surface, the vector $\mathbf{d}_3$ being the tangent of the centreline $\mathbf{r}(s)$,

$$\begin{aligned} \mathbf{r}'(s) &= \mathbf{d}_3(s) \\ &= \mathcal{R}(s)\,\mathbf{e}_z, \end{aligned} \tag{1}$$

where $\mathbf{e}_z$ is the third vector of the 3D canonical basis. Similarly to Kirchhoff rods, the SO_3 structure of the material frame $\mathcal{R}(s)$ yields the existence of a so-called Darboux vector $\Omega(s) = \kappa_1(s)\mathbf{d}_1(s) + \kappa_2(s)\mathbf{d}_2(s) + \kappa_3(s)\mathbf{d}_3(s)$ dictating the space evolution of $\mathcal{R}$ as the so-called *Darboux problem*,

$$\mathcal{R}'(s) = \mathcal{R}(s)\,[\boldsymbol{\kappa}]_\times, \tag{2}$$

where $[\boldsymbol{\kappa}]_\times$ is the skew-symmetric matrix of the 3D curvature vector $\boldsymbol{\kappa}(s) = \{\kappa_1(s), \kappa_2(s), \kappa_3(s)\}$ [Charrondière et al. 2020, Section 2.2].

Unlike Kirchhoff rods though, our choice of ribbon model imposes further constraints on the curvatures. In particular, disregarding geodesic curvature yields $\kappa_2 = 0$. The only remaining quantity allowing for bending of the ribbon surface is $\kappa_1(s) = \kappa(s)$, which is the *normal curvature* of the surface. Finally, the second non-vanishing scalar function $\kappa_3(s)$, which allows the ribbon to twist, is referred to as the *geodesic torsion* of the ribbon. We explain in the following how the geodesic torsion relates to the normal curvature and to the ruling parametrisation of the mid-surface.

Developable surfaces being ruled surfaces, there is a set of rulings spanning the surface of the ribbon. The direction of each ruling $\mathbf{q}$ varies with the function η and is defined by

$$\mathbf{q}(s) = \mathbf{d}_1(s) + \eta(s)\mathbf{d}_3(s). \tag{3}$$

This vector is not unit length and the corresponding ruling segment is $\left\{\mathbf{r}(s) + t\,\mathbf{q}(s),\ t \in [-\frac{w}{2}, \frac{w}{2}]\right\}$, see e.g [Charrondière et al. 2020; Dias and Audoly 2015]. From (3) we have $\eta(s) = \tan\theta(s)$, with $\theta(s)$ being the angle between the ruling $\mathbf{q}$ and the first frame vector $\mathbf{d}_1$ at arc length s. We stress here that the rulings are *not* material lines drawn on top of the ribbon surface: in contrast they change direction as the curvature of the ribbon surface evolves, to always follow a straight path.

As shown in [Dias and Audoly 2015], the developability of the mid-surface imposes the geodesic torsion $\kappa_3(s)$ to be equal to the product $\kappa(s)\eta(s)$, which corresponds to enforcing a vanishing Gauss curvature. We are thus left with two scalar functions for representing the exact degrees of freedom of the ribbon kinematics: $\kappa(s)$ and $\eta(s)$. Furthermore, as explained e.g., in [Charrondière et al. 2020; Dias and Audoly 2015], for the rulings not to intersect each other on the ribbon surface, we need to enforce the so-called Wunderlich constraint,

$$|w\,\eta'(s)| \leq 2, \tag{4}$$

for $s \in [0, L]$.

Finally, the Darboux vector can be written as $\Omega(s) = \kappa(s)\mathbf{q}(s)$ and the Darboux problem (2) simplified as

$$\mathcal{R}'(s) = \mathcal{R}(s)\begin{pmatrix} 0 & -\kappa(s)\,\eta(s) & 0 \\ \kappa(s)\eta(s) & 0 & -\kappa(s) \\ 0 & \kappa(s) & 0 \end{pmatrix}, \tag{5}$$

which together with Equation (1) and the initial values $\mathbf{r}(0)$, $\mathcal{R}(0)$ uniquely generate the shape of the deformed surface of the ribbon.

Note that for the sake of simplicity, it is common to draw the ribbon shape using the rulings [Charrondière et al. 2020; Dias and Audoly 2015], thereby yielding a trapezoidal shape at the boundaries. One possible drawback is that at the $s = 0$ and $s = L$ extremities, the ribbon edges may appear slanted, see Figure 28, top, in the clamped-clamped case (with unconstrained $\eta(L)$) and Figure 3 in the clamped-free case (out of equilibrium solution). However, this skewed boundary issue disappears in the clamped-clamped case in which $\eta(0)$ and $\eta(L)$ are set to zero, see Figure 28, middle. Similarly, this issue is naturally fixed in the clamped-free case as

$\eta(L)$ vanishes at equilibrium due to the absence of external torque at $s = L$. For these reasons, we found that implementing the exact surface at the boundary, which is possible[2] though non-trivial, was not necessary in this article.

Elastic energy. To enrich the model, the ribbon can have some natural normal curvature $\check{\kappa}$ (see Figure 1, left). Following [Dias and Audoly 2015, Section 6.1], the Wunderlich elastic energy of a rectangular ribbon with natural normal curvature $\check{\kappa}$ reads

$$E_{\mathcal{W}} = \frac{Dw}{2} \int_0^L \left[\kappa^2 \left(1+\eta^2\right)^2 \psi(w\eta') - 2\check{\kappa}\kappa(1+\nu\eta^2) \right] \mathrm{d}s, \quad (6a)$$

$$\psi(w\eta') = \frac{1}{w\eta'} \log\left(\frac{2+w\eta'}{2-w\eta'}\right), \quad (6b)$$

where $D = \frac{Yh^3}{12(1-\nu^2)}$ is the bending modulus of the surface, Y the Young modulus and ν is the Poisson ratio[3]. In the limit $\eta' w \to 0$, the Wunderlich energy $E_{\mathcal{W}}$ boils down to the (simpler) Sadowsky energy,

$$E_{\mathcal{S}} = \frac{Dw}{2} \int_0^L \kappa^2 \left(1+\eta^2\right)^2 - 2\check{\kappa}\kappa(1+\nu\eta^2)\mathrm{d}s, \quad (7)$$

which, unlike the Wunderlich energy, does not avoid possible crossings of the rulings (no log term). As such, the Sadowsky energy is valid at small widths w only (i.e. when the Wunderlich constraint is inactive). For developable ribbons of moderate to large widths, the Wunderlich model, though more complex to evaluate, should be considered instead.

4.2 Quasi-developable Case

The RibExt model, which accounts for the presence of stretching on the ribbon surface, is an extension of the work of Shield [1992] as it includes twist in addition to bending. Even if the surface of the ribbon is no longer developable and hence no longer contains rulings, we nevertheless keep on using the variable $\eta(s)$, out of convenience. The model, which has been detailed in Audoly and Neukirch [2021], makes use of the curvature $\kappa(s)$ and twist $\eta(s)\,\kappa(s)$ to describe the geometry of the ribbon. Its elastic energy is

$$E_{\mathcal{R}} = \frac{Dw}{2} \int_0^L (1-\nu^2)\kappa^2 \left(1 + \frac{2}{1+\nu}\eta^2 + \frac{\left(\nu+\eta^2\right)^2}{1-\nu^2}\boldsymbol{\phi}(x)\right) \mathrm{d}s. \quad (8a)$$

$$\boldsymbol{\phi}(x) = 1 - \frac{2}{x}\frac{\cosh x - \cos x}{\sinh x + \sin x}, \; x = \left[3(1-\nu^2)\right]^{1/4} \left(\frac{w^2|\kappa|}{h}\right)^{\frac{1}{2}}. \quad (8b)$$

The function $\boldsymbol{\phi}$ takes values in $[0,1)$, increasing monotonically from $\boldsymbol{\phi}(0) = 0$ to $\boldsymbol{\phi}(+\infty) = 1$. On the one hand, when $\boldsymbol{\phi} = 0$, we recover the elastic energy of a Kirchhoff rod with a flat section, having a ratio of twist to bending rigidities equal to $2/(1+\nu)$, see e.g. [Lurie 2005, Chapter 6]. On the other hand, when $\boldsymbol{\phi} = 1$, we recover the elastic energy of a Sadowsky ribbon. The RibExt model can then interpolate between narrow (small width w, hence small $\boldsymbol{\phi}$) and wide (large width w, hence $\boldsymbol{\phi} \simeq 1$) structures, the appropriate measure to decide which behaviour the system is following being the Shield number

$$\mathrm{Sh} = \frac{w^2}{hL} \int_0^L |\kappa(s)|\,\mathrm{d}s\,, \quad (9)$$

with the system being midway between rod and ribbon when $\boldsymbol{\phi} = 0.5$, that is $\mathrm{Sh} \simeq 10$. An important point to stress is that the Shield number depends on the actual equilibrium state of the structure through the local normal curvature $\kappa(s)$. Consequently, a ribbon with a moderate ratio $\frac{w^2}{hL}$ may nevertheless have a small Shield number (and have a rod-like behaviour) if bending is small everywhere, i.e. $|\kappa(s)|\,L \ll 1$ for all s.

4.3 Energy Minimisation

In addition to the elastic deformation energy, we consider the gravity potential energy associated with gravity vector $\mathbf{g}$. To write this potential energy for the ribbon, we use, following [Charrondière et al. 2020], the approximation in which the mass is concentrated on the centreline. Without this approximation, the numerical model may artificially increase η at the extremities to lower the total energy. We obtain

$$\begin{aligned} E_G &= -\int_0^L \rho h w\, \mathbf{r}(s)\cdot\mathbf{g}\,\mathrm{d}s \\ &= -\rho h w \mathbf{g}\cdot\int_0^L \mathbf{r}(s)\,\mathrm{d}s, \end{aligned} \quad (10)$$

where ρ is the density of the material.

We end up with a total potential energy depending on the vector $\mathbf{X} \in \mathbb{R}^n$, which gathers all degrees of freedom

$$E(\mathbf{X}) = E_{\mathrm{el}}(\mathbf{X}) + E_G(\mathbf{X}), \quad (11)$$

where E_{el} stands for either $E_{\mathcal{S}}$, $E_{\mathcal{W}}$ or $E_{\mathcal{R}}$. In the examples, treated in Section 6, the modelling of e.g. the anchoring of the ribbon, or of the contact with obstacles, introduces equality and inequality constraints, $h_j(\mathbf{X}) = 0$ and $g_k(\mathbf{X}) \geq 0$ respectively. The energy (11) is therefore minimised through the use of the Lagrangian

$$\mathcal{L}(\mathbf{X}) = E(\mathbf{X}) - \lambda_j\, h_j(\mathbf{X}) - \mu_k\, g_k(\mathbf{X}), \quad (12)$$

and its associated Kuhn–Tucker conditions for optimality, see e.g. [Luenberger 1973]. In practical examples, we found it convenient to use the Ipopt solver [Wächter and Biegler 2006], which finds local minima of the energy (i.e. stable equilibrium solutions) satisfying both equality and inequality conditions. More precisely, the algorithm relies on the Interior Point Method with adaptive barrier update [Nocedal et al. 2009; Wächter and Biegler 2006]. In this method, a sequence of barrier problems is solved for a decreasing sequence of barrier parameters μ converging to zero. Equivalently, this process can be viewed as solving the primal-dual equations associated to the Lagrangian (12) through homotopy, with a homotopy parameter μ progressively driven towards zero. During homotopy, each regularised problem is (approximately) solved through a damped Newton solver, which in turn requires factorising the Hessian of the ribbon energy at each internal step.

5 Mixed Versus Chained Elements

We present in this section a numerical implementation of the physical models listed in the previous section. This numerical

[2] Ribbon models are 1D Cosserat-type models whose actual section shape is known [Audoly and Neukirch 2021]: at every abscissa s the deformed section in the $(\mathbf{d}_1, \mathbf{d}_2)$ plane could be drawn instead of the straight ruling. In such a case no trapezoidal effect would appear.

[3] Note that for a naturally flat ribbon ($\check{\kappa} = 0$), the parameter ν vanishes from the integral and remains only in the bending modulus.

implementation is based on the earlier work of Charrondière et al. [2020] but brings key new features which enable us to tackle a much wider range of scenarios. The simulator seeks for stable equilibrium configurations through the minimisation of the ribbon energy.

5.1 The Chained Model of Charrondière et al. [2020]

We quickly summarise here the main aspects of the previous model of Charrondière et al. [2020], named here the *chained* model, in order to better emphasise the improvements of our new, so-called *mixed* model. The chained model is a curvature-based approach where the ribbon configuration is completely defined by the two scalar functions $\eta(s)$ and $\kappa(s)$, together with the position $\mathbf{r}(0)$ and orientation $\mathcal{R}(0)$ at the $s = 0$ extremity of the ribbon. We recall that the geodesic curvature of the ribbon is kept zero, see Section 4. Once the normal curvature $\kappa(s)$ and the geodesic torsion $\kappa(s)\,\eta(s)$ are known, the orientation $\mathcal{R}(s)$ and the position $\mathbf{r}(s)$ of the entire ribbon are obtained through integration of the Darboux system (1), (5). In [Charrondière et al. 2020] the ribbon is split into p elements and a piecewise linear discretisation for the $\kappa(s)$ and $\eta(s)$ functions is used over the length of the rod: $\kappa^{(i)} = a^{(i)}s^{(i)} + b^{(i)}$, $\eta^{(i)} = c^{(i)}s^{(i)} + d^{(i)}$, with $s^{(i)} \in [0, L^{(i)}]$ the local arc length, and $L^{(i)}$ the length of element i. With the exception of the first element, continuity of the functions $\eta(s)$ and $\kappa(s)$ imposes the constraints

$$b^{(i+1)} - b^{(i)} - a^{(i)}L^{(i)} = 0, \tag{13a}$$

$$d^{(i+1)} - d^{(i)} - c^{(i)}L^{(i)} = 0, \tag{13b}$$

which are used to replace the $b^{(i)}$ and $d^{(i)}$ variables and we therefore end up in total with only $2+2\,p$ scalar degrees of freedom. Starting with these $2+2\,p$ degrees of freedom and the position $\mathbf{r}(0)$ and orientation $\mathcal{R}(0)$ at $s = 0$, one can integrate the Darboux system successively in each element $i = 0, \ldots, p-1$ using the power series summation algorithm described in [Charrondière et al. 2020] and adapted from [Casati and Bertails-Descoubes 2013]. Consequently the, say, position at the start of element k, is determined from the computation of $\mathbf{r}$ and $\mathcal{R}$ in the previous $k-1$ elements: one obtains a model with chained elements.

The consequence of dealing with such a kinematic chain is a dense Hessian and hence a costly Newton step: As the number p of elements increases, factorising the Hessian (using e.g., a LU or Cholesky factorisation) increases as $O(p^3)$. The chained model has been proven in [Charrondière et al. 2020] to address accurately and efficiently various clamped-free scenarios, but we show here that it poorly scales to a number of elements larger than 20, and fails to cope with clamped-clamped boundary conditions, see Section 5.6 and Figure 6. In contrast, our new mixed model recovers a sparse banded Hessian and thus a linear complexity with the number p of elements. In the Möbius and confined ribbon tests presented in Section 6, the number of elements used was typically $p \sim O(100)$, for a computational cost of a few seconds only.

5.2 Our New Mixed Model

To address the shortcomings of the chained model, and also deal easily with clamped-clamped (see Figure 4) or circular boundary conditions (see Figure 7), or with contact with obstacles (see Figure 13), we introduce a model where elements are independent of each other, even though this means dealing with redundant degrees of freedom. Elements are glued to each other through well-chosen matching constraints, as detailed hereafter.

Independent elements. We consider that for each element i, the two scalars in the normal curvature $\kappa^{(i)} = a^{(i)}s^{(i)}+b^{(i)}$ and the two scalars in the direction $\eta^{(i)} = c^{(i)}s^{(i)} + d^{(i)}$ are degrees of freedom, in addition to the position $\mathbf{r}^{(i)} = \mathbf{r}(s^{(i)} = 0)$ (represented as a 3D vector) and orientation $\mathcal{R}^{(i)} = \mathcal{R}(s^{(i)} = 0)$ (represented by the nine scalar entries of the rotation matrix[4]). For each of the p elements, we thus have 16 scalar degrees of freedom $\mathbf{X}^{(i)} = \{a^{(i)}, b^{(i)}, c^{(i)}, d^{(i)}, \mathbf{r}^{(i)}, \mathcal{R}^{(i)}\}$. In the following we denote by $x_\alpha^{(i)}$ each of the 16 scalar components of $\mathbf{X}^{(i)}$.

The Darboux system (1), (5) can then be integrated locally and independently on each element i using the power series method of Charrondière et al. [2020], starting from the beginning of the element $(\mathbf{r}^{(i)}, \mathcal{R}^{(i)})$. This integration gives the frame $\mathcal{R}^{(i)}(s)$ and the position $\mathbf{r}^{(i)}(s)$ over the element, both of these quantities depending only on the variables local to the element, $\mathbf{X}^{(i)}$.

As a result, the gravitational energy (10), which depends on the centreline position $\mathbf{r}(s)$, can now be decomposed as a sum of local integrals,

$$E_G(\mathbf{X}) = \sum_{i=1}^{p} {E_G}^{(i)}\left(\mathbf{X}^{(i)}\right), \tag{14}$$

$$\text{where } {E_G}^{(i)}\left(\mathbf{X}^{(i)}\right) = -\rho h w \mathbf{g} \cdot \int_0^{L^{(i)}} \mathbf{r}^{(i)}\left(s^{(i)}\right) \mathrm{d}s^{(i)}. \tag{15}$$

Note that each of the gradients of the gravitational energy $\frac{\partial E_G}{\partial x_\alpha^{(j)}}$ with respect to each of the 16 degrees of freedom $x_\alpha^{(j)}$ of the j^{th} element only depends on the local variable $\mathbf{X}^{(j)}$, i.e. $\frac{\partial E_G}{\partial x_\alpha^{(j)}}(\mathbf{X}) = \frac{\partial {E_G}^{(j)}}{\partial x_\alpha^{(j)}}(\mathbf{X}^{(j)})$. This is in contrast with the chained model, for which $\frac{\partial E_G}{\partial x_{\mathrm{r}}^{(i)}}$ depends on all previous elements $j \le i$ (with $x_{\mathrm{r}}^{(i)}$ standing for the 2 reduced degrees of freedom $a^{(i)}$ and $c^{(i)}$ of element i in the chained model).

Looking now at the Hessian matrix of the gravitational energy, it is noteworthy that $\frac{\partial^2 E_G}{\partial x_\alpha^{(j)} \partial x_\beta^{(k)}}$ vanishes if $j \neq k$. The consequence is that only the 16×16 blocks $\frac{\partial^2 E_G}{\partial x_\alpha^{(j)} \partial x_\beta^{(j)}}(\mathbf{X}) = \frac{\partial^2 {E_G}^{(j)}}{\partial x_\alpha^{(j)} \partial x_\beta^{(j)}}(\mathbf{X}^{(j)})$ located on the diagonal of the Hessian are non-zero. Again, this is a major difference with the Hessian of the gravitational energy for the chained model, which turns out to be dense.

Finally, as the elastic energy $E_{\mathrm{el}}(\mathbf{X})$ only depends on the curvature $\kappa(s)$ and the ruling direction $\eta(s)$, it is trivially decomposed into a sum of local energies $E_{\mathrm{el}}^{(i)}(\mathbf{X}^{(i)})$. Similarly to the gravitational energy, the corresponding Hessian is banded (with an even thin-

[4] We follow the choice of Casati and Bertails-Descoubes [2013] to represent frames as 3×3 matrices, and do not use a reduced parametrisation such as quaternions. The reason is that we want to preserve the linearity of Equation (1) with respect to $\mathcal{R}$, which is key to the power series integration of the Darboux problem [Casati and Bertails-Descoubes 2013, Theorem 1]. As explained in [Casati 2015, Remark 4.1.14], using quaternions would break linearity, hence compromising the effectiveness of the power series integration scheme.

ner band of width 4). Therefore, the Hessian of the total energy $\frac{\partial^2 E}{\partial x_\alpha^{(j)} \partial x_\beta^{(k)}}(\mathbf{X})$ is banded.

As in [Charrondière et al. 2020], the gradient and Hessian terms can be computed by power series integration, as the applicability of the summation algorithm of Casati and Bertails-Descoubes [2013] propagates through differentiation with respect to $\mathbf{X}$ and through integration with respect to s. For instance, the (generalised to 3D) gradient $\nabla\mathbf{r}(s,\mathbf{X}) = \frac{\partial \mathbf{r}}{\partial \mathbf{X}}(s,\mathbf{X})$ admits a power series whose recurrence is simply obtained by differentiating the recurrence formula for $\mathbf{r}(s)$ obtained from Darboux integration. Its integral $\int_0^L \frac{\partial \mathbf{r}}{\partial \mathbf{X}}(s,\mathbf{X})ds$ over the centreline results from a simple integration of the corresponding power series, which is similar to polynomial integration. Besides, implementing all these computations turns out to be much simpler in the mixed case compared to the chained model, as all required quantities can be decomposed locally over each element.

To form consistent elements smoothly connected to each other, we use the two high-order continuity conditions (13). Furthermore, as described below, we introduce six orthonormality constraints to enforce the frames at the start of each element $\mathcal{R}^{(i)}$ to belong to $\mathcal{SO}_3$, as well as six matching constraints to connect element frames and positions together. Since all the added constraints only involve one or two elements, the Hessian of the Lagrangian (12), which is the matrix eventually inverted in the Newton step, *remains banded*. Here again, the gradient and Hessian of the Lagrangian are computed locally using power series integration.

Orthonormality constraints. The six quadratic orthonormality conditions express the fact that the matrix $\mathcal{R}^{(i)}(s^{(i)}=0)$ describing the orientation of the three Cosserat directors (which are its columns) has to be a rotation matrix, i.e. to belong to $\mathcal{SO}_3$,

$$\mathcal{R}^{(i)}(s^{(i)}=0)|_k \cdot \mathcal{R}^{(i)}(s^{(i)}=0)|_k = 1 \quad \forall k \in \{1,2,3\}, \tag{16a}$$

$$\mathcal{R}^{(i)}(s^{(i)}=0)|_k \cdot \mathcal{R}^{(i)}(s^{(i)}=0)|_{k+1 \bmod 3} = 0 \; \forall k \in \{1,2,3\}, \tag{16b}$$

where $\mathcal{M}|_k$ stands for the k^{th} column of matrix $\mathcal{M}$.

Matching constraints. The six matching conditions express the continuity of the position and orientation between the end of element $i-1$ and the start of element i,

$$\mathbf{r}^{(i-1)}(s^{(i-1)}=L^{(i-1)}) = \mathbf{r}^{(i)}(s^{(i)}=0), \tag{17a}$$

$$\mathcal{R}^{(i-1)}(s^{(i-1)}=L^{(i-1)})|_k \cdot \mathcal{R}^{(i)}(s^{(i)}=0)|_{k+1 mod\, 3} = 0 \; \forall k \in \{1,2,3\}. \tag{17b}$$

Conditions (13)-(16)-(17) are added as equality constraints in the energy minimisation procedure when we look for a stable equilibrium solution, see Section 4.3.

In the rest of this section, we discuss our choice for (17b), already used in [Sonneville and Brüls 2014], for identifying two rotation matrices. Indeed this identification has the minor issue of non uniqueness. In essence we want the three column vectors $\mathbf{a}$, $\mathbf{b}$, $\mathbf{c}$ of the first matrix to be identical to the 3 column vectors $\mathbf{d}$, $\mathbf{e}$, $\mathbf{f}$ of the second matrix. Conditions (17b) have the solution $\mathbf{a}=\mathbf{d}$, $\mathbf{b}=\mathbf{e}$, $\mathbf{c}=\mathbf{f}$, but also $\mathbf{a}=\mathbf{d}$, $\mathbf{b}=-\mathbf{e}$, $\mathbf{c}=-\mathbf{f}$ for example.

We briefly discuss below two alternative choices and show they are actually much more problematic. A first alternative would be

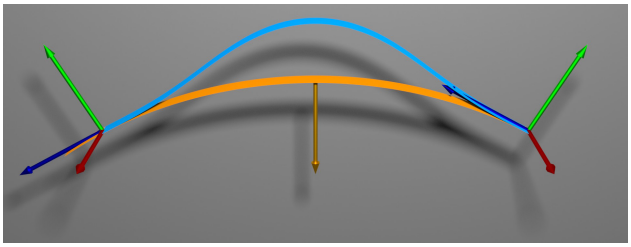

Fig. 4. A simple clamped-clamped experiment. The orange ribbon describes a perfectly circular arc and serves as a warmstart for the minimisation algorithm. This warmstart shape is clamped at the right end, but not at the left end. The two frames are indicating the clamping constraints, and the orange arrow indicates the gravity direction. The blue ribbon is the result of the constrained minimisation. For this experiment, we have used $\frac{w}{L} = \frac{1}{11}$, $\Gamma = 100$, $\nu = 0.35$.

to replace (17b) with

$$\mathcal{R}^{(i-1)}(s^{(i-1)}=L^{(i-1)})|_k \cdot \mathcal{R}^{(i)}(s^{(i)}=0)|_k = 1 \quad \forall k \in \{1,2,3\}. \tag{18}$$

In such a case, the minimisation routine adds a Lagrange multiplier λ_j to each constraint $h_j(\mathbf{X}) = 0 = \mathcal{R}^{(i-1)}(s^{(i-1)} = L^{(i-1)})|_{1,2,3} \cdot \mathcal{R}^{(i)}(s^{(i)}=0)|_{1,2,3} - 1$, for $j = 1,\dots,p-1$, where the vector $\mathbf{X} \in \mathbb{R}^n$ gathers all degrees of freedom, see (12). The first order optimality conditions is then a system for the unknowns $\mathbf{X}$ and λ_j which takes the form

$$\nabla\mathcal{L}(\mathbf{X}) = 0, \tag{19}$$

$$h_j(\mathbf{X}) = 0. \tag{20}$$

The key point is now to realise that this system is singular on any solution $\mathbf{X}=\mathbf{X}^\star$. Indeed, on the solution the three column vectors of $\mathcal{R}^{(i-1)}(s^{(i-1)}=L^{(i-1)})$ are equal to those of $\mathcal{R}^{(i)}(s^{(i)}=0)$ and they have unit norm. The optimality condition writes $\nabla\mathcal{L}(\mathbf{X}^\star) = 0 = \nabla E(\mathbf{X}^\star) - \lambda_j \nabla h_j(\mathbf{X}^\star)$ and at $\mathbf{X}=\mathbf{X}^\star$, $\nabla h_j(\mathbf{X}^\star) = 0$ because it is the derivative of the square of a normalised vector[5]. Having $\nabla h_j(\mathbf{X}^\star) = 0$ clearly prevents us from finding the associated Lagrange multiplier λ_j.

A second alternative would be to replace (17b) with the 9 conditions equating each element of $\mathcal{R}^{(i-1)}(s^{(i-1)}=L^{(i-1)})$ with the corresponding element of $\mathcal{R}^{(i)}(s^{(i)}=0)$. Because the column vectors of each matrix are linked by orthonormality conditions, these 9 conditions are not independent. Therefore the gradient of the Newton method associated with the first order optimality conditions becomes singular.

In practice, the non uniqueness issue of (17b) is avoided by choosing close-enough warmstarts in the minimisation procedures. For example if we are looking for a ribbon equilibrium where the $s=L$ extremity is rotated by a large amount, we are going to start with the untwisted solution and find solutions for a series of intermediate problems where the rotation is gradually increased and each solution is used to warmstart the minimisation procedure when looking for the next solution (the solution with

[5] We consider $\mathbf{u}(\alpha) \in \mathbb{R}^n$ a normalised vector function of a scalar α. We take the squared norm $\|\mathbf{u}(\alpha)\|^2 = 1$ and differentiate it with respect to α. We find $\mathbf{u}(\alpha) \cdot \frac{d\mathbf{u}(\alpha)}{d\alpha} = 0$.

increased rotation). This type of approach is reminiscent of path following algorithms.

5.3 Clamping Conditions

If the ribbon is clamped at its $s = 0$ extremity, its position $\mathbf{r}(0)$ and orientation $\mathcal{R}(0)$ should match those of the clamping. One could filter out the corresponding degrees of freedom or add constraints as in (17). The chained model uses the filtering. For the mixed model, we have tried both and found the same efficiency for both solutions. Since filtering degree of freedom involves restructuring the matrices, we chose to keep the 12 degrees of freedom in $\mathbf{r}(0)$ and $\mathcal{R}(0)$ and enforce the constraints

$$\mathbf{r}^{(0)}(s^0 = 0) - \mathbf{r}_{\text{clamp}} = 0, \tag{21a}$$

$$\mathcal{R}^{(0)}_{i,j}(s^{(0)} = 0) - \mathcal{R}_{\text{clamp}\,i,j} = 0 \quad \forall i,j \in \{1,2,3\}. \tag{21b}$$

Clamping a ribbon at the end ($s = L$) is achieved, for both the chained and the mixed model, with the same approach as in (17)

$$\mathbf{r}^{(p-1)}(s^{p-1} = L^{(p-1)}) - \mathbf{r}_{\text{clamp}'} = 0, \tag{22a}$$

$$\mathcal{R}^{(p-1)}(s^{(p-1)} = L^{(p-1)})|_k \cdot \mathcal{R}_{\text{clamp}'}|_{k+1\,mod\,3} = 0 \quad \forall k \in \{1,2,3\}. \tag{22b}$$

As in the matching of elements, these clamping conditions suffer from non uniqueness of solutions, but are fixed by using good enough warmstarts.

5.4 Circular Boundary Conditions

In Section 7, to study a Möbius configuration resting on an horizontal support in the presence of gravity, we introduce circular boundary conditions in the same spirit as (21) and (22)

$$\mathbf{r}^{(p-1)}(s^{p-1} = L^{(p-1)}) - \mathbf{r}^{(0)}(s^0 = 0) = 0, \tag{23a}$$

$$\mathcal{R}^{(p-1)}(s^{(p-1)} = L^{(p-1)})|_k \cdot \mathcal{R}^{(0)}(s^{(0)} = 0)|_{k+1\,mod\,3} = 0 \quad \forall k \in \{1,2,3\}. \tag{23b}$$

Three different invariances can then arise in the mathematical optimisation problem: (i) a translational invariance, (ii) a rotation invariance, and (iii) a $s \to s + \Delta s$ invariance. Each of these invariances renders the gradient of the Newton routine involved in the minimisation procedure singular (zero eigenvalue(s)). We found it convenient to kill the translation invariance by either prescribing the position of the center of mass of the ribbon or its $s = 0$ point. Owing to the powerful treatment of singular gradient matrices by Ipopt, see [Wächter and Biegler 2006], we did not need to kill the rotation invariance. The $s \to s + \Delta s$ invariance is also easily reduced by requiring some special point of the ribbon to be at $s = 0$.

5.5 Contact Handling

We introduce the possibility for the ribbon to come to contact with one or more planes, and we use the position degrees of freedom of the mixed model to handle it. The contact constraint is tested at the start of each element and the end of the last element, i.e., for $s = s_c \in \{0, L^{(1)}, L^{(1)} + L^{(2)}, \ldots, L - L^{(p-1)}, L\}$, and written for the two extremities $C_\pm$ of each ruling passing through the centreline points $\mathbf{r}(s_c)$, i.e., for

$$\mathbf{r}_{c_\pm} = \mathbf{r}(s_c) \pm \frac{w}{2}\,\mathbf{q}(s_c), \tag{24}$$

see Figure 3. If we want to restrict the ribbon to be outside the half space delimited by the plane passing through point A with outward normal $\mathbf{n}$, for each of the $2(p+1)$ points $C_\pm$ we write the condition

$$\left(\mathbf{r}_{c_\pm} - \mathbf{r}_A\right) \cdot \mathbf{n} \geq 0. \tag{25}$$

As these contact conditions are written directly with the degrees of freedom of the model, the cost for computing the Lagrangian and its first and second derivatives stays linear in the number of elements. For this reason, if we want to refine the contact treatment, we think preferable to increase the number p of elements rather than introducing second order points $C_\pm$ (at the middle of the elements for example).

5.6 Efficiency of the Mixed Model

The chained model of Charrondière et al. [2020] has a dense energy Hessian, making its inversion cubic with respect to the number of elements p. The cubic complexity of chained models was already illustrated in the case of super-clothoids [Casati and Bertails-Descoubes 2013, Fig. 9]. In contrast, the introduction of the variables $\mathbf{r}^{(i)}$ and $\mathcal{R}^{(i)}$ in the mixed model makes the system sparse, and as all constraints only involve one or two elements, its Hessian matrix is essentially banded. This allows us to recover a *linear* computation complexity of the system with respect to p. In practice, the mixed model becomes quicker to solve than the chained model as soon as there are more than $p \approx 20$ elements, see Figure 5. It is moreover worth noting that although there are more variables in the mixed model than in the chained model, from a developer point of view, the former is easier to implement compared to the latter, and less error prone.

We illustrate the efficiency of the mixed model over the chained model on two scenarios using the Sadowsky and Wunderlich energies. The first scenario consists in computing the equilibrium of a ribbon hanging under gravity and allows to check the theoretical complexity. The second scenario is more complex as we clamp both extremities of the ribbon and leads to a failure of the chained model. We nondimensionalise the system with D and L to maximise the efficiency of the solver, leaving only two parameters: (i) the weight $\Gamma = \frac{\rho h^2 g L^3}{D}$, and (ii) Poisson's ratio ν. The gravity acceleration vector is written $\mathbf{g} = -g\,\mathbf{e}_g$, with $\mathbf{e}_g$ a unit vector along the vertical direction.

Clamped-free Scenario. We consider a ribbon of length $L = 1$, width $w = 0.1$, bending rigidity $D = 1$, Poisson's ratio $\nu = 0.35$, and weight $\Gamma = 30$. The vertical direction is set such that $\mathbf{e}_g = \mathbf{e}_z$, and the ribbon is clamped with a tilt of 0.2 radians in the $(\mathbf{e}_y, \mathbf{e}_z)$ plane, with horizontal direction $\mathbf{d}_1(0) = \mathbf{e}_x$. The warmstart for the minimisation procedure is chosen to be an almost flat ribbon $\kappa(s) = 10^{-5}s + 10^{-4}$, $\eta(s) = 10^{-5}s + 10^{-4}$. We measure the computing time for Ipopt to converge when using 10, 20, 40 and 100 elements, for both Sadowsky and Wunderlich energies. The equilibrium is shown in the inset of Figure 5.

The results displayed in Figure 5 match the expected costs, cubic for the chained model and linear for the mixed model, and show that in this example the energy used has little influence on the computation time. The larger number of degrees of freedom of the mixed model causes a larger prefactor in its computation time, and consequently, for a small number of elements, here less than 20, the

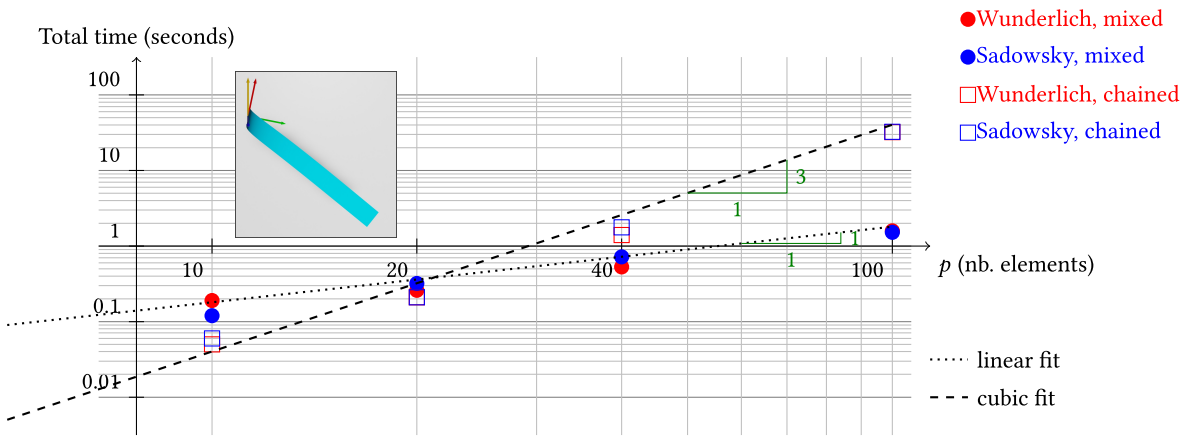

Fig. 5. Efficiency of the mixed and chained models in the Clamped-free scenario of Section 5.6. Computation times are reported and linear and cubic interpolations are shown. The ribbon is hanged under gravity, with a clamping orientation tilted with regard to the gravity vector (inset figure, yellow arrow indicates vertical direction). The mixed model is more efficient when the number of elements is greater than 20 and follows a linear time cost. The chained model is valuable when no more than 20 elements are used, but its time cost increases rapidly, following a cubic trend.

chained model appears to be faster. However, beyond 20 elements, the mixed model clearly offers better performance.

Clamped-clamped Scenario. We now consider a ribbon of length $L = 1$, width $w = 0.01$, bending rigidity $D = 1$, Poisson's ratio $\nu = 0.5$, and weight $\Gamma = 100$. We fix the gravity direction such that $\mathbf{e}_g = \mathbf{e}_z$ and clamp the ribbon vertically at one end and horizontally at the other. Distance between clamping points is set to 0.95. The warmstart is here also an almost flat ribbon : $\kappa(s) = 10^{-4}s + 10^{-3}$, $\eta(s) = 10^{-4}s + 10^{-3}$. We use Sadowsky and Wunderlich energies, and compute the equilibrium with 10, 20 and 40 elements. The equilibrium is shown in the inset of Figure 6.

Computation times are displayed in Figure 6. Even with 1000 iterations (i.e., roughly 1000 seconds), the solver does not converge with the chained model. The mixed model converges in a few seconds and shows little dependency on the number of elements, although it is about one order of magnitude longer than in the Clamped-free Scenario. Note that the warmstart configuration does not respect the end clamp, which is rotated by an angle of $\frac{\pi}{2}$ radian with regard to the $s = 0$ clamp. This scenario shows that clamping the end of a ribbon is not a trivial task.

6 Verification and Validation

So far we have built an efficient numerical model for a developable (inextensible) ribbon, which turns out to be an order of magnitude faster compared to the chained model of Charrondière et al. [2020], while maintaining the same level of accuracy. In addition, unlike the latter model, ours can be easily coupled to bilateral and unilateral constraints, which widens the range of scenarios one can simulate. These novel possibilities open the doors for an insightful evaluation of our numerical model, relying upon the simulation of demanding scenarios.

The rest of the article is aimed at evaluating our model meticulously under two different angles, following the early distinction made in software reliability [Boehm 1981; Pham 2006]:

— *Numerical verification*: are we building the numerics right? That is, given a reduced physical model for an inextensible ribbon (Sadowsky or Wunderlich), how well does our numerical model solve these equations? How *accurate* is it? How much computational time does it require to reach a given accuracy? How does it compare to alternative numerical methods for solving the Sadowsky and Wunderlich equations, in terms of accuracy and efficiency?
— *Physical validation*: are we building numerics for the right physical model? That is, given our goal to predict the mechanics of *real* strip-like objects for designing purposes, how relevant is the reduced, inextensible ribbon model we are building upon? How *realistic* is it? What is its validity range? How does it compared with alternate physical models, like thin plates or thin rods?

To answer these fundamental questions, we propose in the following to compare our numerical model to theoretical, numerical, and experimental predictions, on a set of challenging scenarios.

Comparison benchmark. Our numerical model comprises so far two different variants: Merci-Sadowsky, which simulates the statics of Sadowsky ribbons, limited to small widths only, and Merci-Wunderlich, which uses the (extended) Wunderlich energy, suitable for small to large widths.

To verify and validate our numerical model (the two variants Merci-Sadowsky and Merci-Wunderlich), we compare it against several reference – analytical or numerical – models in the following:

— MAE: the analytic, Matched Asymptotic Expansion introduced in [Audoly and van der Heijden 2022] in the limit case of a vanishing width, $w \to 0$;
— Sadowsky (shooting): a shooting technique for the Sadowsky ribbon (implemented in Mathematica), based on the works of [Neukirch and Audoly 2021] and [Kumar et al. 2021];
— Wunderlich (shooting): a shooting technique for the Wunderlich ribbon, that we specifically developed for this article using the continuation software Auto (see details in Appendix B).

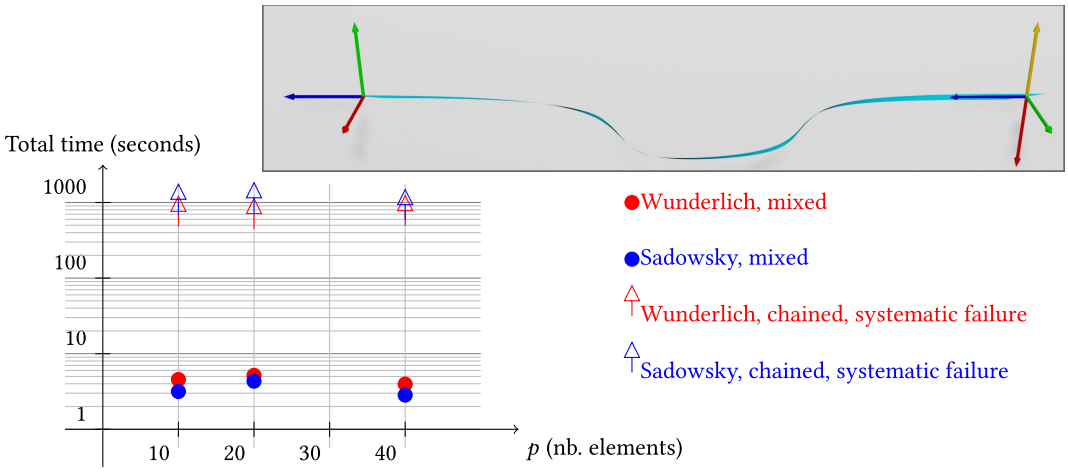

Fig. 6. Efficiency of the chained and mixed models in the Clamped-clamped Scenario of Section 5.6. The chained model always fails with status «Restoration failed» for Wunderlich energy, or reaches the maximum number of iterations (1000) for Sadowsky energy. This demonstrates the usefulness of the mixed model, which converges within a few seconds. Inset figure: yellow arrow indicates vertical direction, while the red, green, blue arrows indicate the orientations at the clamps, showing that one quarter of a turn of end-rotation has been applied on the left clamp.

— DER-Wunderlich: a free implementation of the Wunderlich model based on the DER model [Korner et al. 2021], available at https://data.caltech.edu/records/2147.
— FEniCS-Shell: a 2D plate model, relying on Naghdi's nonlinear shell theory [Naghdi 1963], and implemented in the free FEniCS finite elements suite [Habera et al. 2018; Hale et al. 2018].

The first three methods, based on asymptotic expansions or shooting techniques, are highly popular in Physics, and will serve in the remainder of the article as *reference* models for *verifying the accuracy* of our approach in challenging scenarios. In contrast, DER-Wunderlich, which relies on a popular position-based algorithm of Computer Graphics, will be used to showcase the *computational advantage* of our mixed approach combining curvature-based elements with position-based joints. Finally, FEniCS-Shell will serve as a reference implementation of a more general, 2D mechanical model, for *validating* the reduced physics upon which our numerical model is based.

Our validation and verification study is conducted on three distinct scenarios: 1/ The Möbius band (Section 7), 2/ The buckling of a 2D confined ribbon (Section 8), and 3/ The Lateral Buckling test (Section 9). Each case is analysed physically and numerically in depth. These three sections can be read in any order, as they are pretty independent of each other. The reader who is pressed for time might even skip the first two ones and jump directly to Section 9 which leverages yet another (slightly extensible) physical model for the ribbon.

7 The Möbius Band Scenario: Accuracy at a Competitive Cost

A popular test case from physics and mechanics, for which multiple theoretical and numerical results have been derived based on the theory of developable ribbons – Sadowsky and Wunderlich – is the *Möbius band*, illustrated in Figure 7, see e.g., [Fosdick and Fried 2015]. Though simple in appearance (everyone can make a Möbius band by twisting a paper strip and gluing its extremities), this scenario is actually extremely challenging to simulate due to the presence of a singularity point at the surface of the ribbon [Bartels and Hornung 2015]. This singularity fails to be captured using the Kirchhoff rod theory, which highlights a major difference between ribbon and rod models' predictions [Huang et al. 2020; Kumar et al. 2020]. A second interesting point is that a developable solution for a Möbius strip mathematically exists for a large range of widths, more precisely as long as the width of the ribbon does not exceed $\frac{L}{\sqrt{3}}$ [Schwarz 1990]. As such, the Möbius band represents a relevant – both demanding and useful – test for the *numerical verification* of our developable solver. It should be noted that a recent experimental work [Kumar et al. 2021], based on an accurate stereo-vision technique for capturing the geometry of a Möbius strip, has confirmed the observations predicted by the developable ribbon theories for moderate to large widths, hence highlighting some physical validity of these models. Evaluating our numerical approach against the Möbius band scenario can thus, to some extent, also be viewed akin to *physical validation*, at least in the range of moderate to large widths.

7.1 Singularity

The difficulty of simulating a Möbius band with the Wunderlich model stems from the singularity occurring in the flat zone of the configuration, at $s = s^*$, where the curvature vanishes and changes sign [Starostin and van der Heijden 2007]. It is noteworthy that such a singularity does not exist with the Kirchhoff rod model [Mahadevan and Keller 1993]. This singularity is surrounded by a small region where both $\kappa(s)$ and $\eta(s)$ vary sharply. The value of the derivative $\eta'(s)$ is regularised by the *Log* term in the Wunderlich energy, which diverges as $w\,\eta'(s) \to \pm 2$. At the singular point $s = s^*$, and for any width w value, the solution nevertheless achieves $w\,\eta'(s^*) = \pm 2$ [Audoly and van der Heijden 2022], making numerical computation difficult. Note that the Wunderlich energy remains finite because $\kappa(s^*) = 0$ and $\kappa^2(s)\,\psi(w\eta'(s)) \to 0$

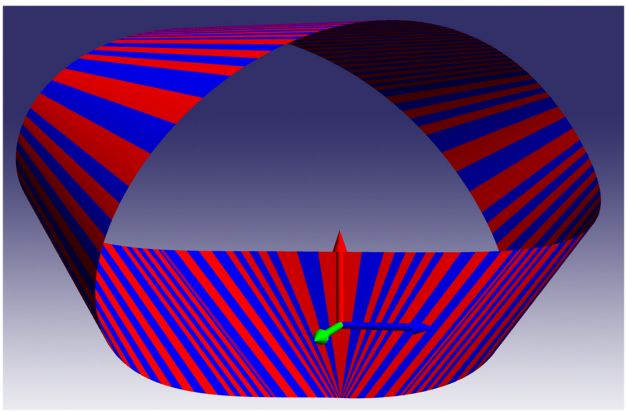

Fig. 7. Möbius solution obtained with Merci-Wunderlich for the normalised width $\frac{w}{L} = 0.1$, and the constraints $\eta(0) = 0 = \eta(L)$. The singular point $s = s^*$ lies at the origin of the cartesian frame. The mesh has been refined so that the increment of the function $\eta(s)$ in any element is not too large, eventually leading to a total number of 169 elements of unequal lengths. The elements are colored alternatively in red and blue, revealing the rulings that lie at the border between two elements.

ALGORITHM 1: Computation of a Möbius Ribbon with Merci

1 `InitialiseRibbon`$(L = 1, w = 0.01, D = 1, \Gamma = 0, p = 65)$;
2 **for** i *de* 1 *à* p **do**
3 `Initialiseelement`$\Big(i, L^{(i)} = \frac{1}{p}, a^{(i)} = 0, b^{(i)} = 2\pi, c^{(i)} = 0, d^{(i)} = 0\Big)$;
4 $\mathcal{F}_0 \leftarrow \begin{pmatrix} 0 & 0 & 1 \\ 1 & 0 & 0 \\ 0 & 1 & 0 \end{pmatrix}$;
5 $\mathbf{p}_0 \leftarrow \begin{pmatrix} 0 & 0 & 0 \end{pmatrix}$;
6 `ConstrainRulesatClamping`$(\eta(0, L) = 0)$;
7 **for** θ *from* 0 *to* π *by increment of* $\frac{\pi}{5}$ **do**
8 $\mathcal{M} \leftarrow \begin{pmatrix} 0 & 0 & 1 \\ \cos(\theta) & -\sin(\theta) & 0 \\ \sin(\theta) & \cos(\theta) & 0 \end{pmatrix}$;
9 `FixBothEndClamping`$(\mathbf{p}_0, \mathcal{F}_0, \mathbf{p}_0, \mathcal{M})$;
10 `CallIpopt`();
11 `ReMesh`();
12 `CallIpopt`();

at the singular point. This difficulty makes ODE or shooting-based approaches ineffective in finding solutions with small values of w, or having the solution going through the singular point: such numerical approaches only compute half the Möbius solution, stopping at the singular point [Moore and Healey 2019; Starostin and van der Heijden 2007, 2015]. Additionally, it is noteworthy that ad-hoc regularisations have been used to smooth the singularity out [Moore and Healey 2019], hence altering the solution close to s^*.

Similarly to the chained model [Charrondière et al. 2020, Section 5.4], our approach is capable of going through singular points. In particular, we show here that it can perfectly cope with the Möbius

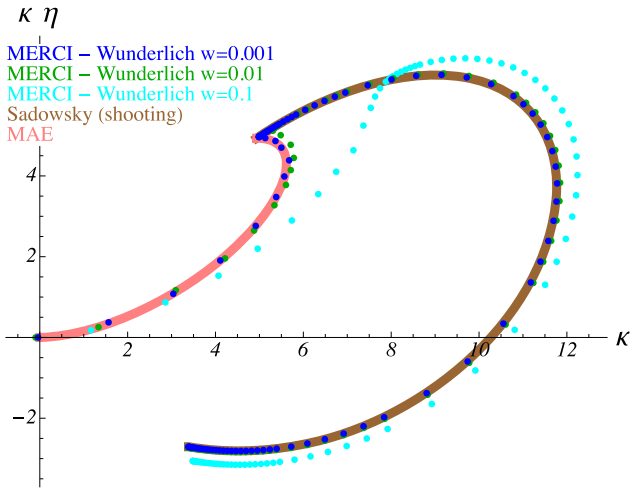

Fig. 8. Parametric plot of the first half of the Möbius solution computed with Merci-Wunderlich for different width values. We also show the Sadowsky (shooting) solution in brown (Merci-Sadowsky giving exactly the same result) and inner layer of MAE in pink, illustrating the convergence of our Merci-Wunderlich code as $w \to 0$.

singularity, and we use MAE, i.e. the asymptotic limit ($w \to 0$) of Audoly and van der Heijden [2022], to verify our results.

7.2 Simulation Protocol

We build the Möbius solution following the procedure described in Algorithm 1. The problem is nondimensionalised by setting the total contour length of the ribbon $L = 1$ and the bending rigidity $D = 1$, a choice which can be made without loss of generality (see [Romero et al. 2021] for more information on nondimensionalisation). We start with a limited number $p = 65$ of elements (line 1) and refine the mesh later (line 11). The remeshing, which simply consists in adding or removing elements based on the gradient of the solution, brings up the number of elements typically between $p = 150$ to $p = 200$. We initialise the ribbon with an untwisted and circular shape (lines 2-3). The $s = 0$ end is clamped at the origin with the material frame aligned with the axes of the reference frame (lines 4-5). The $s = 1$ end is also clamped at the origin, and its material frame is gradually rotated (lines 7-10). After each rotation step, the minimisation routine is called (line 10). Please note that we constrain the rulings at the clamps, $s = 0, L$ to be aligned with the clamps, i.e. orthogonal to the tangent. This constraint reads $\eta(0) = 0 = \eta(L)$ and ensures that the section of the ribbon is flat when entering the clamp (line 6). In Appendix C we show other ways to constrain the function $\eta(s)$ at boundary points $s = 0, L$.

We have run this algorithm with Merci-Wunderlich for several width values and observed a 100% convergence success, each step requiring around 20 to 40 iterations in Ipopt and the whole process taking about a minute on a standard laptop. It is also possible to obtain the Möbius configuration without the rotation procedure if one warm-starts the minimisation procedure with $\kappa(s) = 2\pi$ and $\tau(s) = \cos 2\pi s$, a process that we call Merci-Wunderlich-OneShot (see supplementary material). Figure 7 shows a converged Möbius configuration with $w = 0.08$ and a refined mesh near the singular point.

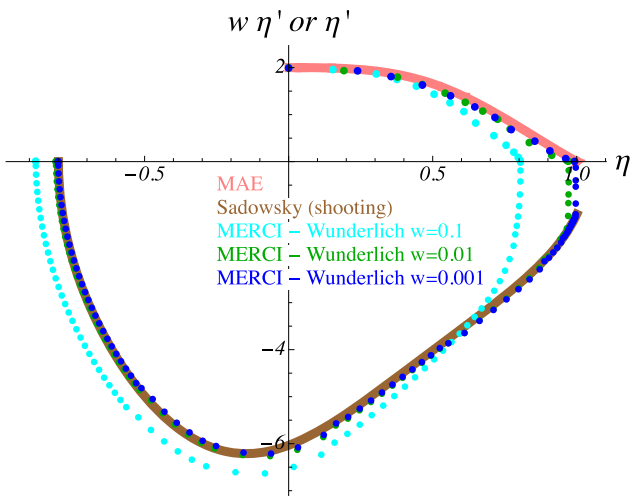

Fig. 9. First half of the Möbius solution computed with MERCI-WUNDERLICH for different width values. We also show the SADOWSKY (shooting) solution in brown (MERCI-SADOWSKY giving exactly the same result) and inner layer of the Matched Asymptotic Expansion (MAE) in pink. The vertical axis plots $\eta'(s)$ when $\eta'(s) < 0$ and $w\,\eta'(s)$ when $\eta'(s) > 0$.

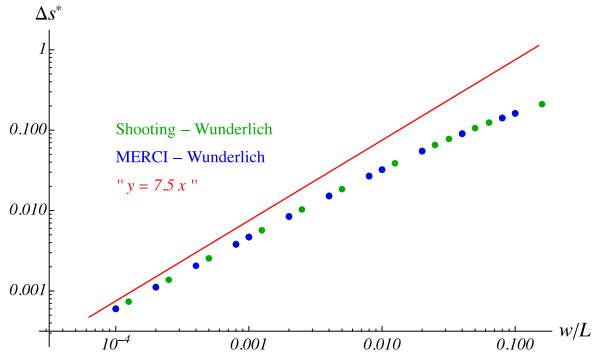

Fig. 10. Size $\Delta s^\star$ of the singular region, where the orientation of the rulings quickly varies (i.e. the inner layer in the Matched Asymptotic Expansion (MAE) calculations). The red line, $y = 7.5\,x$, approximately fits the asymptote of the Wunderlich curve as $w \to 0$.

7.3 Accuracy Results

We now make a few remarks about these Möbius solutions. As explained in [Freddi et al. 2016; Neukirch and Audoly 2021] the ribbon solutions must have $|\eta(s)| < 1$, $\forall s$, and this is what we find here, see Figures 8 and 9. For all width values considered, we find that $w\,\eta' = \pm 2$ at the singular point, see Figure 9. We also find that as $w \to 0$, the solution approaches the asymptotic solution MAE presented in [Audoly and van der Heijden 2022]. More precisely, Figure 9 shows only half ($s \in [0, \frac{1}{2}]$) of the Möbius solution with the vertical axis plotting $\eta'(s)$ when $\eta'(s) < 0$ and plotting $w\,\eta'(s)$ when $\eta'(s) > 0$. This choice clearly illustrates the two regions in the Möbius solution when $w \to 0$: (i) the Sadowsky solution for the outer region (far from the singularity) in which $\eta'(s) < 0$, and (ii) the asymptotic expansion solution (see Appendix B and [Audoly and van der Heijden 2022]) for the inner region (around the singularity) in which $\eta(s)$ increases quickly from 0, with $|\eta'(s)| \gg 1$. We define the size $\Delta s^\star$ of the singular region as twice the arc length spent above the horizontal axis in Figure 9. This corresponds to all the points where ($\eta'(s) > 0$ and $s < \frac{1}{2}$) $\bigcup$ ($\eta'(s) < 0$ and $s > \frac{1}{2}$). The dependence of $\Delta s^\star$ on the width w is plotted in Figure 10. Please note that the clamping constraints on the position, frame, and η, may be removed and replaced by periodic constraints, as we will see in Section 7.5.

7.4 Performance Comparison with DER

In Section 5.6, we have already demonstrated the computational advantage of our mixed curvature-position formulation over a fully reduced (purely curvature-based) formulation. Now we wish to assess how our mixed formulation compares to a more classical, position-based approach where the centreline is modelled explicitly by a dense set of nodes. We especially focus on the popular DER model [Bergou et al. 2010], which has recently been extended to a position-based discrete Wunderlich model [Huang et al. 2022; Korner et al. 2021] and numerically verified against the Möbius band scenario.

In the following, we thoroughly compare our approach with such a DER-like ribbon model on the Möbius test, in terms of accuracy and efficiency. In our comparison, we use the reference C++ implementation of Korner et al. [2021]'s model, named DER-WUNDERLICH hereafter, which is publicly available at https://data.caltech.edu/records/2147. Similarly to our MERCI algorithm, DER-WUNDERLICH solves the static ribbon problem by minimising the Wunderlich energy under kinematic constraints using a second order method leveraging the Hessian of the energy. However, due to their very different choice of degrees of freedom (nodal positions, twist angles, and discrete η over the centreline), their constraints are aimed at enforcing the inextensibility of the centreline as well as the developability of the mid-surface. Instead, recall that in our case, inextensibility and developability are intrinsically taken into account over each element by our specific choice of degrees of freedom. Our sole constraints are aimed at gluing elements together and enforcing material frames to lie in SO_3. Another difference lies in the choice of the optimisation solver. Theirs is based on Sequential Quadratic Programming (in-house implementation based on sparse linear algebra), which approximates the dual unconstrained problem as a sequence of quadratic objectives. In contrast, ours relies on the Interior Point method (IPOPT implementation), which constructs a sequence of approximated dual unconstrained problems with barrier functions. That said, both solvers structurally resemble each other in the sense that they boil down to iterations over Newton–Raphson steps constructed from the factorisation of a banded Hessian.

We run MERCI-WUNDERLICH following both Algorithm 1 and its one-shot variant MERCI-WUNDERLICH-ONESHOT (see supplementary material). We run DER-WUNDERLICH on the original Möbius PYTHON script used to produce the results of Korner et al. [2021, Figure 5.4], and for the sake of fairness we made a few straightforward optimisations (such as reducing the number of unnecessary iterations) so as to improve its overall efficiency. In supplementary material we distribute the input files and/or scripts used for our Möbius comparison, for both MERCI-WUNDERLICH and DER-WUNDERLICH. Our tests were all run on the same standard laptop featuring a 64-bit, 3GHz, processor.

Our target test consists of a Möbius band of length $L = 1$ and width $w = 0.1$ (see Figure 7), a scenario which falls in the range of examples studied in [Korner et al. 2021]. We focus on the $\eta(s)$ solution recovered by Merci-Wunderlich and DER-Wunderlich. Using Auto with extreme spatial refinement (700 discretisation points), we first compute a *reference* solution for $\eta(s)$, noted $\eta^\star(s)$. As the result of a converging process combined to spatial interpolation, this reference solution can be safely considered to be very close to the exact solution at any point $s \in [0, 1]$. We then compare this reference $\eta^\star(s)$ with the discrete output $\bar{\eta}_p(s_i)$ of Merci-Wunderlich (respectively of DER-Wunderlich), produced at discrete arc lengths $s_i, i \in \{1..p\}$ for a given number p of elements. While p is varied (from $p = 10$ to $p = 250$), the accuracy ε_p is computed as the discrete L_1-norm of the difference between $\eta^\star$ and each approximation $\bar{\eta}_p$, $\varepsilon_p = \frac{1}{p}\sum_{i=1}^{p} |\eta^\star(s_i) - \bar{\eta}_p(s_i)|$. Accuracy and timing results for Merci-Wunderlich and DER-Wunderlich are presented in Figure 12. The shapes of the resulting Möbius ribbons obtained for the same time budget of a few seconds are visually compared in Figure 11.

As expected from a curvature-based formulation, and already demonstrated in [Casati and Bertails-Descoubes 2013, Fig. 9] when comparing super-clothoids to DER, we observe in Figure 12(a) a *superior convergence order* (quadratic instead of linear for our curvature measure) ribbon model compared to DER-Wunderlich.

In addition to this higher-order accuracy, it is noteworthy in Figure 12(b) that our Merci-Wunderlich code is *significantly more efficient* than DER-Wunderlich for any spatial resolution p. Several factors explain this computational gain. First, as already showcased in Section 5.6, one key result of our Merci approach is precisely to improve considerably the *complexity* of original chained curvature-based models, thanks to a *mixed* curvature/position-based formulation. Similarly to Figure 5, the slope of Merci-Wunderlich in Figure 12(b) is no longer cubic but turns out to be almost linear[6] w.r.t. the resolution p – due to a Hessian that is banded instead of dense. A similar order is found for DER-Wunderlich. Second, it is noteworthy that the Merci-Wunderlich curve is substantially shifted below the DER-Wunderlich curve, corresponding to a steady ×10 speed gain. This difference is amplified again (around ×2.5) when using our so-called Merci-Wunderlich-OneShot algorithm, which cleverly warmstarts the problem (see supplementary material). By examining carefully Korner et al. [2021]'s algorithm, we have noted that their overall complexity scales roughly as $(N_1 + N_2 + N_3)\,p$ where p is the number of elements, and N_i the number of iterations required at the i^{th} step of the algorithm. The first and second steps are common to our method: they consist in increasing the ribbon curvature to form a circle and twist both ends, respectively. However, we remark that DER-Wunderlich requires *regularising* the problem to help continuation, by adding a small term proportional to $\eta''(s)$. This term is eventually removed to obtain the final solution. In addition, for DER-Wunderlich to achieve the equilibrium

[6] As the resolution p exceeds 50, we note that Merci rather scales as p^q with $q \approx 1.5$ for Merci-Wunderlich and $q \approx 1.25$ for Merci-Wunderlich-OneShot. This is explained by the slightly higher number of inner iterations requested for Ipopt to converge at large p. We note a similar behaviour for DER-Wunderlich, with $q \approx 1.75$.

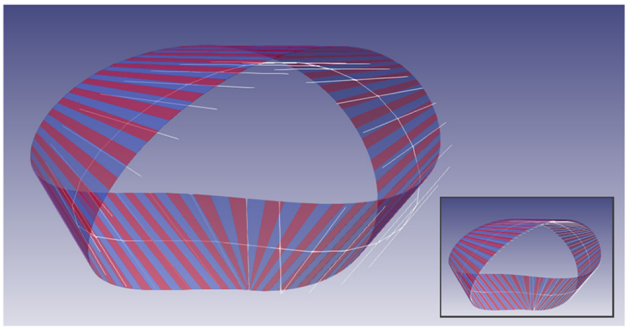

Fig. 11. Resulting shape of the Möbius ribbon, computed with either Merci-Wunderlich (blue/red coloured elements) or DER-Wunderlich (white rulings), for the same time budget ($t = 3.8$ s) on the same machine. The limited precision that is affordable by DER-Wunderlich ($\varepsilon_p = 5.10^{-2}$ against $\varepsilon_p = 6.10^{-4}$ for Merci-Wunderlich) yields a clear visual shift of the geometry of the ribbon. When increasing the resolution of DER-Wunderlich, the resulting shape ends up converging towards the Merci shape, although at a much higher cost (bottom-right inset: 100 elements for both models, DER-Wunderlich is now 6.7 times more costly, albeit 25 times less accurate, than Merci for the prediction of the ruling angles).

of moderately wide ribbons ($\frac{w}{L} > 0.05$, which is our case here), the width w needs to be set to a thinner value and then progressively increased. These two simplifications of the numerical problem are at the origin of a third continuation step, whose goal is to remove progressively such approximations. For each algorithm, we set each N_i at its minimal possible value to ensure proper achievement of the Möbius band configuration. These values, which are almost independent of the number p of elements, are very different depending on the algorithm used, as summarised in Table 1. In particular, our algorithm requires much less iterations for the two first steps than DER-Wunderlich. Moreover, as it does not require any regularisation nor any artificial ribbon thinning, the third step is bypassed. Remarking that each iteration takes approximately the same time for both methods, we conclude that the extra cost of DER-Wunderlich mainly comes from these extra continuation steps necessary to achieve the Möbius band configuration.

All in all, as shown in Figure 12(c), because our method takes a mixed approach between curvature-based and position-based models, it offers a *highly competitive* alternative to DER-Wunderlich in terms of accuracy vs. cost. Our model does not only yield a correct visual geometry much faster than DER-Wunderlich, as illustrated in Figure 11, but it also proves able to reach very high accuracies ($\varepsilon_p < 10^{-3}$) that remain inaccessible for DER-Wunderlich.

7.5 Extension to Contact Under Gravity

At this stage, we are convinced that our model is able to solve the Wunderlich model in a very accurate, fast, and robust way. With this calibration at hand, we go one step further by adding gravity and contact to the Möbius band.

We stress that doing such a challenging experiment would be extremely difficult if not impossible with shooting codes of the literature, including the ones that we have included in our benchmark (Sadowsky (shooting) and Wunderlich (shooting)).

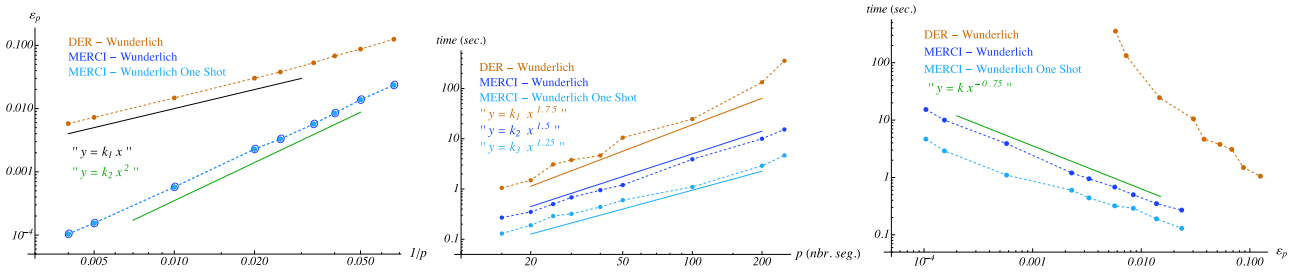

Fig. 12. Comparison between Merci-Wunderlich and DER-Wunderlich on the Möbius test, in terms of accuracy and efficiency. Left (log-log scale): Resulting accuracy ε_p of the Möbius band reached for p elements, function of the length $\frac{1}{p}$ of each element. Middle (log-log scale): Computational time for reaching the Möbius band configuration, function of the number p of elements. Right (log-log scale): Cross-referencing the two left plots, one obtains the computational time required to achieve a given accuracy ε (regardless of p), for each tested algorithm.

Table 1. Number of Continuation Iterations Required for Each Step of the Möbius Algorithm: 1/ Curvature Increase from Flat to Circular, 2/ Twist of Both Ends, and 3/ Removal of Energy Regularisation and Artificial Ribbon Thinning

Möbius algorithm	N_1	N_2	N_3
DER-Wunderlich [Korner et al. 2021]	7	35	30
Merci-Wunderlich (Algorithm 1)	1	5	0
Merci-Wunderlich-OneShot (Supp. mat.)	0	1	0

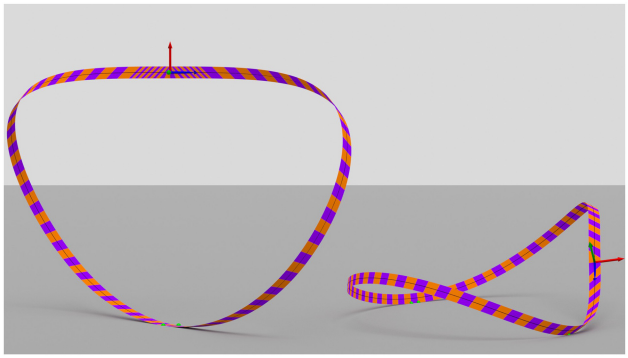

Fig. 13. (Left) the heavy Möbius ribbon stands up on a plane, or (right) the ribbon falls on its side, both solutions being stable. Parameters are $\Gamma = 0.1$ and $\frac{w}{L} = 0.01$.

With our Merci code, this experiment is simple to perform and only takes a few seconds to be computed (see also the script in the supplementary material).

We assume the Möbius ribbon to rest on a rigid planar support, the direction of gravity being normal to the plane. Thanks to our numerical model, we find out that two possible configurations exist: (i) the ribbon stands up, or (ii) the ribbon falls on its side. To compute these configurations, we start with the weightless Möbius solution obtained in previous Section and add the planar obstacle with the help of an inequality constraint, see Section 5.5. The clamping conditions (21)-(22) with $\mathbf{r}_{\text{clamp}} = \mathbf{p}_0 = \mathbf{r}_{\text{clamp}'}$ and $\mathcal{R}_{\text{clamp}} \cdot \mathcal{F}_0 = 0 = \mathcal{R}_{\text{clamp}'} \cdot \mathcal{F}_0$ (see Algorithm 1) are removed and replaced by cyclic conditions (23). Finally, to kill the translational invariance, we add the condition that the center of mass of the ribbon lies on an axis defined with the normal to the plane support

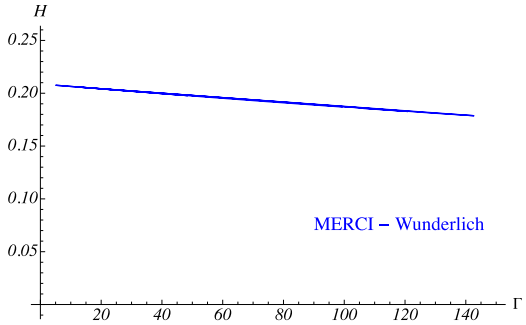

Fig. 14. Height of the Möbius configuration as a function of the weight Γ, for $\frac{w}{L} = 0.025$.

and the origin of the global frame. We do not kill the rotation invariance and therefore the configurations shown in Figure 13 can be freely rotated around the vertical axis. We keep the condition $\eta(0) = 0 = \eta(L)$ in order to kill the invariance $s \longrightarrow s + \Delta s$ (though convergence was also achieved with the condition $\eta(0) = -\eta(L)$), hence the singular point stays at $s = 0$. We obtain two kinds of local minima (i.e. stable equilibria) of the energy, see Figure 13 and the supplementary material. The standing-up configuration has its singular point lying at the top of the configuration, and we stress that this configuration seems to exist and be stable for a wide range of widths w and weight Γ values, see Figure 14 where we plotted the height of the solution as a function of the weight Γ. It seems that the standing-up configuration is stabilised from side tilt by the 4 contact points on the edge of the ribbon, and from rolling by the following argument. In the continuous limit (with infinitely small elements), the Möbius configuration is in contact with the plane along the ruling at the bottom point, $s = L/2$, which means that it could roll in the direction perpendicular to this ruling. Rolling is energetically favorable if it lowers the center of mass in the gravity field. To test this, we have to compute the curvature $\kappa^{\perp}$ of the ribbon surface in the direction perpendicular to the ruling (please note that the curvature in the direction of the ruling is zero by definition). In the $(\mathbf{d}_1, \mathbf{d}_3)$ frame, the curvature matrix is given by [Dias and Audoly 2015],

$$\begin{pmatrix} \kappa & -\eta\,\kappa \\ -\eta\,\kappa & \eta^2\,\kappa \end{pmatrix}_{(\mathbf{d}_1, \mathbf{d}_3)}. \tag{26}$$

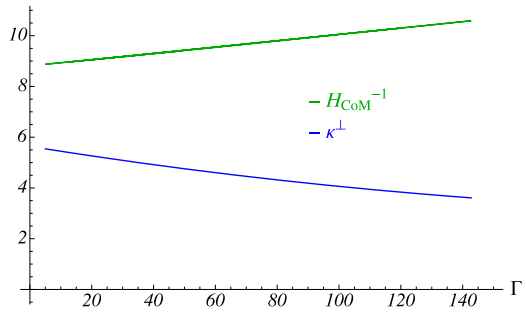

Fig. 15. Is the Möbius ribbon going to roll? Comparison between the distance of the center of mass from the plane, H_{CoM}, and the curvature $\kappa^{\perp}$ of the ribbon surface in the direction perpendicular to the ruling at the contact point with the support. ($\frac{w}{L} = 0.025$)

If we rotate this matrix by an angle $\theta = \arctan \eta$ we obtain

$$\begin{pmatrix} \kappa\,(1+\eta^2) & 0 \\ 0 & 0 \end{pmatrix}_{(\mathbf{ruling}^{\perp},\mathbf{ruling})}. \tag{27}$$

Hence we have $\kappa^{\perp} = \kappa\,(1+\eta^2)$. We note H_{CoM} the distance from the plane to the center of mass, and have the condition that if $\kappa^{\perp} > 1/H_{\mathrm{CoM}}$, the ribbon spontaneously rolls. We plot $\kappa^{\perp}$ and $1/H_{\mathrm{CoM}}$ as functions of Γ in Figure 15 and see that this condition is never reached. By warm-starting the min-search procedure, we can nevertheless obtain configurations where the ribbon lies on its side with two contact regions, see Figure 13-right. Finally, we note that for width values $w < 0.1$ the width only plays a minor role here, as it does not change the stability property of the solution and only slightly changes the curve $H(\Gamma)$.

Of course our contacting Möbius experiment would deserve to be fully validated on experiments and/or theory – which, to the best of our knowledge, do not exist currently. That said, this numerical experiment illustrates the capacity of our numerical model to help investigate new and challenging scenarios. In the following, we specifically verify and validate our code on one of the few well-studied experiments involving an elastic ribbon and contact: the confined ribbon buckling experiment [Roman and Pocheau 1999], exhibiting a complex cascade of (2D) folds.

8 The (2D) Confined Ribbon Experiment: Capture of Subtle Buckling Cascades

We consider a planar experiment where the ribbon is forced to buckle between two rigid planes, see Figure 16. Due to its resemblance with the Euler Buckling experiment (a straight planar rod compressed at both ends), this experiment has been coined *Constrained Euler Buckling* [Domokos et al. 1997]. It was extensively studied by Roman and Pocheau [1999] who proposed a classification for the possible configurations and examined their self-similarity properties [Pocheau and Roman 2004; Roman and Pocheau 2002]. More recently, this problem has been reopened in the perspective of the wrinkling of confined elastic structures [Tzokova 2020]. Confined buckling of plates and cables has numerous industrial applications, for example oil-drilling [Miller et al. 2015; Thompson et al. 2012] or thin-walled or lightweight structures for civil engineering [Bradshaw et al. 2002].

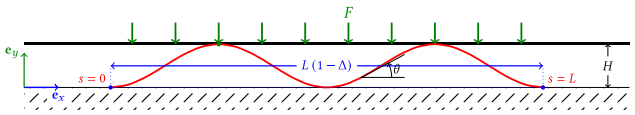

Fig. 16. Setup for the confined ribbon buckling experiment. A ribbon is clamped at both extremities ($s = 0$ and $s = L$) on a first plate, lying at $y = 0$. As the distance $L(1-\Delta)$ between the two clamps is less than L, the ribbon buckles. A second plate, at $y = H$, constrains the vertical span of the buckled configuration and generate folds. The total vertical compression force applied on the upper plate is noted F.

Here, based on the Roman and Pocheau [2002] scaling, we derive specifically a semi-analytical model for the fold cascade, so as to validate our numerical model precisely.

8.1 Semi-analytical Solution

We consider a ribbon of length L, width w, flexural rigidity D, clamped at both extremities $s = 0$ and $s = L$. The distance between the two clamps is $L\,(1-\Delta)$. The ribbon is also confined between two horizontal walls separated by a distance H, see figure 16. Through non-dimensionalisation, we use L as unit length and Dw/L^2 as unit force, that is we set (with no loss of generality) $L = 1$ and $Dw = 1$ in the code. We fix the value of Δ (in the interval $0.05 \leq \Delta \leq 0.3$) and gradually decrease H. If $H > H_0(\Delta)$ the upper plate is too high to generate any contact. We compute the value $H_0(\Delta)$ from the planar Elastica solution [Bigoni 2012; Love 1944]

$$\frac{H_0(\Delta)}{L} = \frac{\sqrt{m}}{K(m)}, \tag{28}$$

where $K(m) = \int_0^{\pi/2} (1 - m\sin^2\theta)^{-\frac{1}{2}}\,d\theta$ is the complete elliptic integral of the first kind, see supplementary material. We find the modulus m by numerically inverting

$$\Delta = 2\left(1 - \frac{E(m)}{K(m)}\right), \tag{29}$$

where $E(m) = \int_0^{\pi/2} (1 - m\sin^2\theta)^{\frac{1}{2}}\,d\theta$ is the complete elliptic integral of the second kind. In the range $\Delta \leq 0.3$, we find that a good interpolation of $H_0(\Delta)$ is given by

$$\frac{H_0(\Delta)}{L} \simeq \frac{2}{\pi}\sqrt{\Delta} - 0.2\,\Delta^{1.5}. \tag{30}$$

8.2 Validation Results

As shown in Figure 17 and in our accompanying video, when H is decreased to values smaller than $H_0(\Delta)$, contact arises. First, contact occurs only along a ruling (i.e. for an isolated value of s), a situation which has been called *lineic contact* by Roman and Pocheau [2002]. As we go on decreasing H, the contact force F, from the upper wall to the ribbon, increases. When H reaches a threshold value, the contact region extends and *planar contact* appears (i.e., for values of s inside an interval). As H is further lowered, a snap instability is reached where the contact force drops abruptly and a new fold appears, hanging between the two walls. For these *hanging fold* configurations, the contact force decreases as H is lowered. The contact force eventually reaches zero when the lowest point of the fold touches the lower wall. We are now back with a lineic

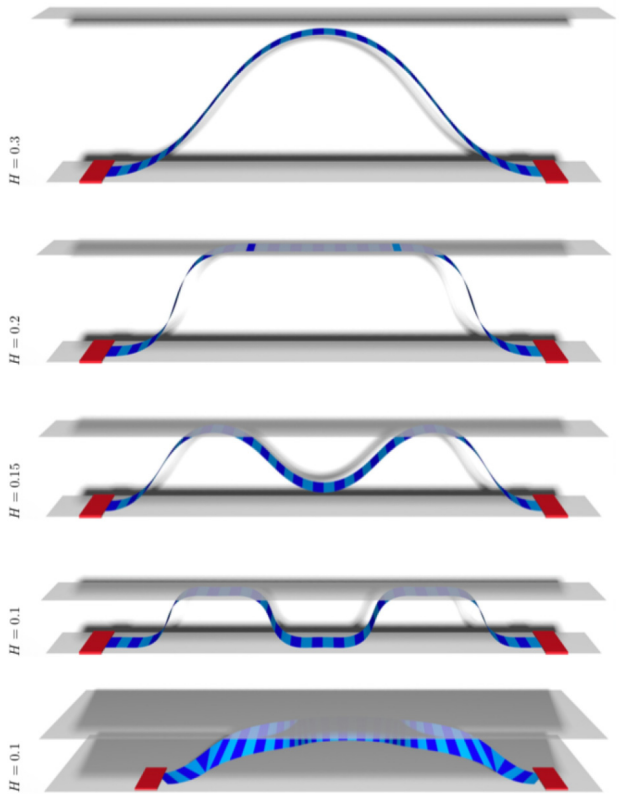

Fig. 17. Different configurations for the confined ribbon experiment simulated with our MERCI code. From top to bottom: vertically unconstrained planar Elastica ($\Delta = 0.2$ and $H = 0.3$), planar contact with $n = 1$ ($\Delta = 0.2$ and $H = 0.2$), hanging fold with $n = 2$ ($\Delta = 0.2$ and $H = 0.15$), planar contact with $n = 2$ ($\Delta = 0.2$ and $H = 0.1$), and a 3D configuration exhibiting twist and singular points at which $|w\,\eta'(s)| = 2$ ($\Delta = 0.3$ and $H = 0.1$). We use $\frac{w}{L} = 1/20$, and we work with the Wunderlich model without constraining η at the clamps. Note that a small amount of self-weight Mg is used, such that $\Gamma = Mg/(Dw/L^2) = 10$.

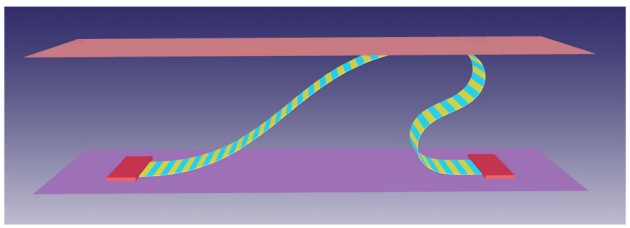

Fig. 18. We retrieve the *Spiral* configuration recently characterised experimentally by Deboeuf et al. [2024] in the confined ribbon experiment, for $\frac{H}{L} = 0.22$ and $\Delta = 0.4$.

contact situation, but with 3 isolated s values for which contact occurs.

This scenario repeats itself with ribbon configurations comprising more and more waves, as described in [Roman and Pocheau 2002]. We define the number $n \geq 1$ of waves as half the number of isolated inflexional points along the ribbon, $n = \#\{s_i\}$ such that $\kappa(s_i) = 0$ and $\kappa(s) \neq 0$ for s near s_i. We remark that depending on

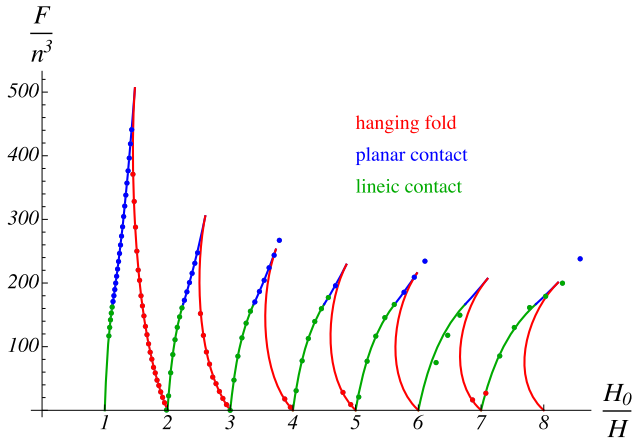

Fig. 19. Total vertical compression force F for $\Delta = 0.2$ and decreasing height H values. The number n of folds is used to rescale the vertical axis and the height H_0 of the first contact is used to rescale the horizontal axis. The agreement between our semi-analytical solution (solid line) and our numerical results (dots) is excellent.

$\frac{w}{L}$, $\frac{H}{L}$, and Δ, 3D solutions with twist might pop up, see the last configuration in Figure 17. Due to the presence of hysteresis, there are possibly multiple stable equilibrium solutions existing for the same values of $\frac{H}{L}$ and Δ. Additionally, for large Δ value (typically $\Delta > 0.3$) we found S-shaped solutions, see Figure 18. These solutions have been reported experimentally by Deboeuf et al. [2024] and called *Spiral* configurations, see also [Chai 2006].

Contact is treated with inequality constraints ($y \geq 0$ and $y \leq H$) in our numerical setup and the total vertical compression force F is extracted as the sum of the active Lagrange multipliers associated with the constraint $y \leq H$. The force F depends on n, $\frac{H}{L}$, and Δ. To validate our numerical results, we compare the computed values of the force F against our analytical model in Figure 19, for $\Delta = 0.2$ and for up to $n = 7$ folds. We observe an excellent agreement between the two.

In addition, we show in Appendix A how the curves for the lineic and planar contact can be rescaled to a single (yet approximate) master curve given by

$$\frac{F}{H_0\,(10\,n)^3} = 9\left(1 - \frac{n\,H}{H_0}\right) - 39\left(1 - \frac{n\,H}{H_0}\right)^2 + 92\left(1 - \frac{n\,H}{H_0}\right)^3, \quad (31)$$

valid for all n, Δ, and $\frac{H}{L}$, thereby generalizing the scaling introduced by Roman and Pocheau [1999].

9 Extension to Quasi-developable Ribbons

The different models considered so far (Sadowsky, Wunderlich) make the assumption that the surface of the ribbon does not extend nor compress, being hence restricted to a developable surface since the initial configuration is planar (rectangular). While for some scenarios, this inextensible assumption has been shown to correctly describe the physics of the ribbon [Kumar et al. 2021, 2020], in some other cases extensibility plays a key role in the deformation of the ribbon [Audoly and Neukirch 2021; Romero et al. 2021]. Examples where the ribbon is not a developable surface include the twisted straight ribbon [Audoly and Neukirch 2021; Chopin et al.

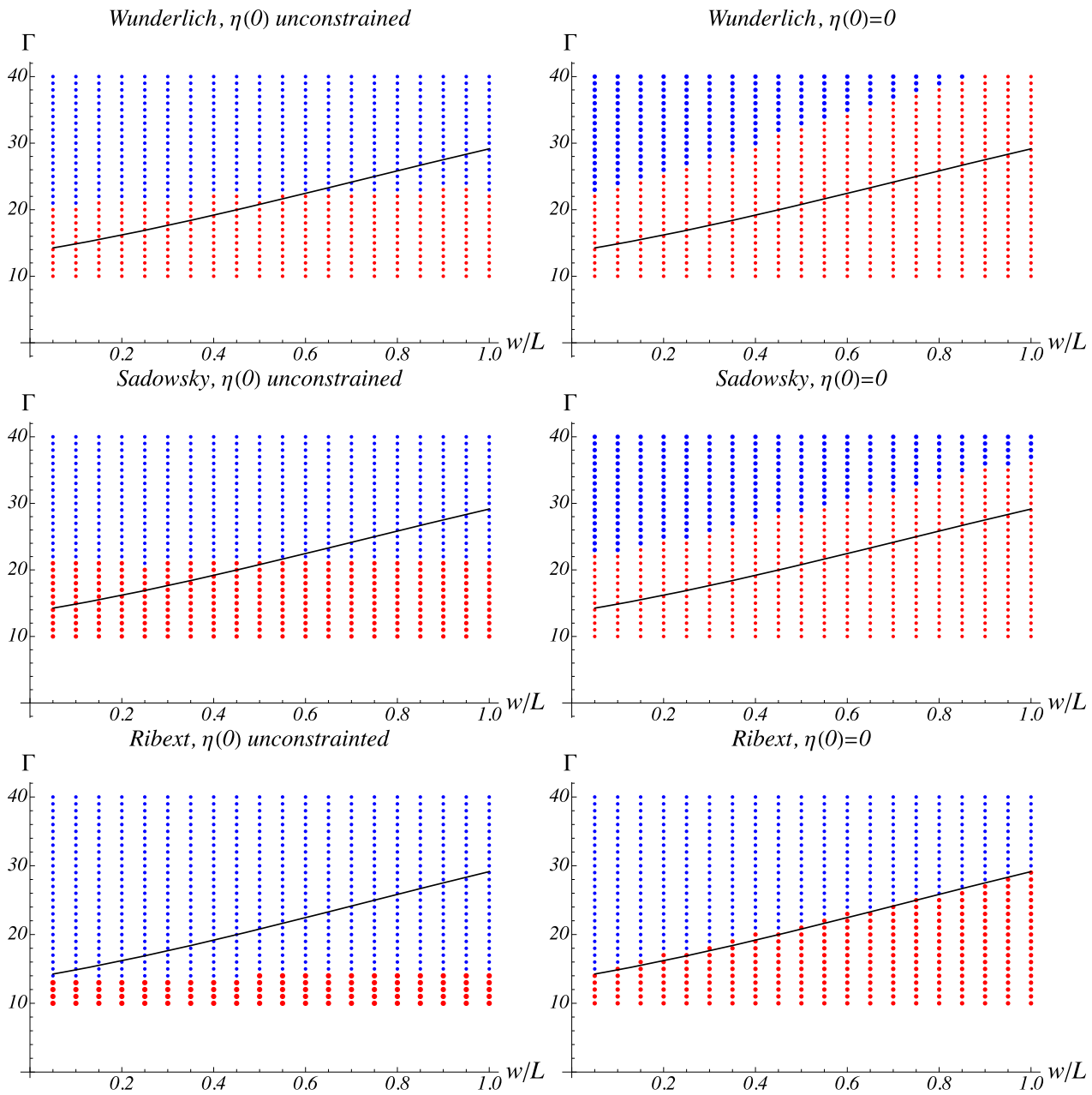

Fig. 20. Results for the Merci code on the LTB test. This test, introduced in [Romero et al. 2021], studies the threshold between (unbuckled) 2D configurations and (buckled) 3D configurations. The reference curve is drawn black and we colorcode 2D configurations in red and 3D configurations in blue. The left column reports runs where the clamp constraint $\eta(0) = 0$ has not been enforced. Our Merci-Ribext implementation, with $\eta(0) = 0$, successfully passes this 3D test. (Note that all six cases have been performed with the constraint $|w\,\eta'(s)| \leq 2\ \forall s$ on).

2015], or the lateral buckling experiment [Michell 1899; Reissner 1989; Romero et al. 2021] for which Sadowsky and Wunderlich models both fail to predict the correct buckling threshold.

9.1 Validation Failure

The chained Wunderlich ribbon model of Charrondière et al. [2020] has already been shown to fail to capture the correct threshold of the lateral buckling instability in [Romero et al. 2021, Figure 9(a)]. Of course switching to a mixed formulation does not change this fundamental modelling issue: we confirm and reproduce this failure with our Merci-Wunderlich code in Figure 20, top panel.

This section is dedicated to the enhancement of the underlying physical ribbon model in Merci, in order to fix the buckling threshold issue and increase the applicability range of our simulator. To this aim we devise a new numerical scheme to implement

and integrate the extensible ribbon model [Audoly and Neukirch 2021] – called hereafter MERCI-RIBEXT – in our MERCI code. We compare this extension on the lateral buckling experiment against our two developable ribbon variants MERCI-SADOWSKY and MERCI-WUNDERLICH, and to the 2D plate model FENICS-SHELL.

9.2 Implementation of the RIBEXT Energy in MERCI

Recall that the RIBEXT energy is provided in Section 4.2. The numerical evaluation of the function $\boldsymbol{\phi}(x)$, given in Equation (8b), suffers from catastrophic cancellation when $|x|$ is smaller than 0.01. We, therefore, opt for the use of a Padé approximant to replace $\boldsymbol{\phi}$ in the code, with $\boldsymbol{\phi}_{\text{pade}}(x) = A(x)/B(x)$, $deg(A) = deg(B) = 4\,i$, and i a strictly positive integer, see Section E or Appendix B of [Audoly and Neukirch 2021]. For $i = 1$, $\boldsymbol{\phi}_{\text{pade}}(x) = x^4/(180 + x^4)$ yields the same ribbon energy as in [Sano and Wada 2019], but the results presented here have been computed with $i = 3$.

Another issue with the RIBEXT model is the difficulty to integrate (8a) (as well as its gradient and its Hessian) in closed form. We, therefore, integrate it numerically through the trapezoidal ruling, each element being regularly partitioned into 2^k subintervals, to obtain the approximation $a_k \simeq E_{\mathcal{R}}$. We select the integer k through an incremental test: we first evaluate a_4 and a_5 then, as long as $|a_{k+1} - a_k| > \epsilon$, we increment k. To avoid lengthy computations, we restrict to $k \leq 24$. For performance, a_{k+1} reuses the computation of a_k, allowing to compute $a_1, \ldots, a_k$ with 2^k evaluations of the integrand of $E_{\mathcal{R}}$. This procedure works in general, even if in some cases, the result may be non-accurate due to some specificity of the integrand. Also, the computation cost can sometimes increase due to a potentially high number of evaluations ($2^{24} \sim 10^7$).

9.3 Lateral Torsional Buckling Scenario

We choose the **lateral torsional buckling (LTB)** problem as a test experiment to validate the RIBEXT model and its implementation in MERCI. We consider a thin plate (length L, width w, thickness h) clamped at one edge and subject to its own weight. The clamp orientation is chosen in such a way that gravity is acting against the strong flexural rigidity of the plate so that the sagging cantilever geometry is not produced, see Figure 23. We choose L as unit length and D/L as unit force. This choice is translated by setting $L = 1$ and $D = 1$ in the codes. We fix Poisson's ratio $\nu = 0.35$ and the thickness $\frac{h}{L} = 10^{-3}$, a value small enough to have negligible shear strain through the thickness of the plate.

9.4 Comparison Results

We vary the width $\frac{w}{L}$ and the non-dimensionalised weight of the plate

$$\Gamma = \frac{\text{Mass}\, g}{Dw/L^2} = \frac{\rho g h w L}{Dw/L^2}. \tag{32}$$

When no weight is present ($\Gamma = 0$), the plate lies flat, aligned with the clamp direction. As the weight Γ is increased, the plate stays planar and only slightly sags: the curvature energy remains zero, $E_{bend} = 0$, but a small amount of extension energy E_{ext} is now present, yielding the ratio $E_{ext}/(E_{ext} + E_{bend}) = 1$. As the weight exceeds a threshold value, $\Gamma > \Gamma^*(\frac{w}{L}, \nu)$, the plate buckles on its left (or right) side and curvature arises. In Figure 21

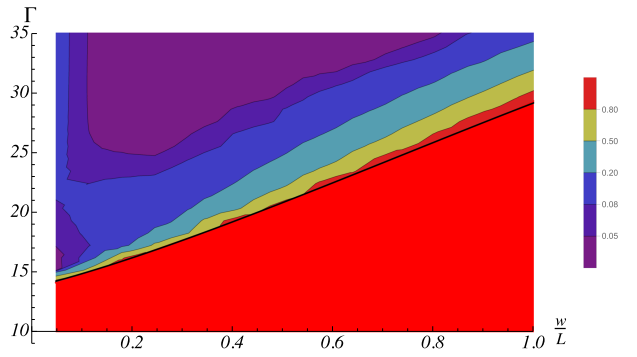

Fig. 21. Contour plot of the energy ratio $E_{ext}/(E_{ext} + E_{bend})$ computed with the FENICS-SHELL code. Before buckling (under the black curve), only stretching is present. After buckling (above the black curve) there are large parts of the diagram where the extension energy is at least 5% of the total deformation energy.

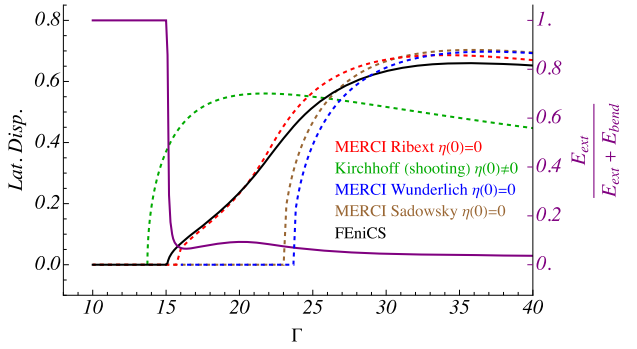

Fig. 22. Lateral Torsional Buckling bifurcation curve with $\nu = 0.35$, $\frac{w}{L} = 0.1$, and $\frac{h}{L} = 0.001$. Note that in the MERCI-SADOWSKY and MERCI-WUNDERLICH codes, the constraints $\eta(0) = 0$ and $|w\eta'| \leq 2$ have been applied. We also plot in purple the ratio of extension energy computed with the FENICS-SHELL code.

we show a contour plot of the energy ratio $E_{ext}/(E_{ext} + E_{bend})$, computed with our reference code FENICS-SHELL, in the plane $(\frac{w}{L}, \Gamma)$. We see that, above the frontier curve $\Gamma^*(\frac{w}{L}, \nu)$, there is a non-negligible region of parameters where the extension energy plays an important role. This frontier curve has been used in [Romero et al. 2021] to test numerical models of plates, and it was shown that Sadowsky and Wunderlich implementations in MERCI failed to accurately reproduce the frontier curve. This failure may have two origins: Sadowsky and Wunderlich theories (i) are 1D models and hence by nature cannot thoroughly reproduce this 2D plate test, and (ii) do not allow any stretching of the surface of the ribbon whereas Figure 21 makes it clear that there is stretching in the system, even for large width values ($\frac{w}{L} \simeq 1$). The RIBEXT model is also a 1D model, but its energy is computed so as to take stretching of the surface of the ribbon into account, and we will see that it behaves much better in the LTB test.

First, in Figure 22, we plot the end displacement of the structure as function of the weight Γ, for $\frac{w}{L} = 0.1$. In what follows, we stress that we have imposed the constraints $\eta(0) = 0$ and $|w\eta'(s)| \leq 2$ for all three ribbon models (the version of Figure 22 without the constraint $\eta(0) = 0$ can be found in the supplementary material). The

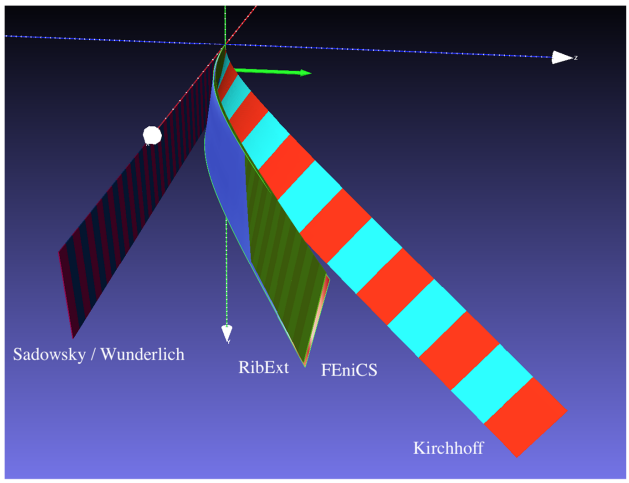

Fig. 23. Equilibrium configurations for the LTB test with $\Gamma = 20$, $\frac{w}{L} = 0.1$, $\frac{h}{L} = 0.001$. While the Sadowsky and Wunderlich models predict an unbuckled shape, the Kirchhoff model predicts a deformation which is too large. Only the RibExt model correctly approximates the reference deformation given by the FEniCS-Shell code.

constraint $\eta(0) = 0$ aligns the rulings of the ribbon surface with the clamp at $s = 0$ and the constraint $|w\eta'(s)| \leq 2$ prevents the rulings to intersect on the surface and to create a singularity. Additionally, we show in Appendix D that just as in the Möbius experiment, the constraint $\eta(0) = 0$ give birth to a boundary layer where $\eta(s)$ varies rapidly in the Wunderlich model. Compared to the FEniCS-Shell output, we see that both Sadowsky and Wunderlich models miss the buckling threshold, but recover a fairly good behaviour at large Γ. Moreover we notice that the discrepancy of these two inextensible models takes place when the extension energy is present in the system, and that the the RibExt model, accordingly, reproduces fairly well the bifurcation curve of the FEniCS-Shell code, see also a comparison of the deformed shapes for the value $\Gamma = 20$ in Figure 23. Please note that here a small value of $\frac{w}{L}$ has been chosen, and that for larger values (e.g., $\frac{w}{L} = 0.4$ in Appendix F) the agreement between RibExt and the FEniCS-Shell code is not as good. Figure 22 also contains the bifurcation curve for the Kirchhoff rod model, which bifurcates too early.

In order to test more thoroughly the three ribbon models (Sadowsky, Wunderlich, and RibExt), we follow the validation procedure introduced in [Romero et al. 2021]. This procedure aims at verifying if a code correctly detects the lateral torsional buckling threshold. Results are shown in Figure 20 where the planar/spatial attribute of the equilibrium shape is color-coded. The color change (i.e. the 2D $\rightarrow$ 3D bifurcation) should happen at the black line which is the reference curve provided in [Romero et al. 2021]. We see that if the constraint $\eta(0) = 0$ is not enforced, the buckling thresholds computed by the three models virtually does not vary with $\frac{w}{L}$ and does not match the reference curve. Once the constraint is enabled, a variation fo the buckling threshold appears, but only the RibExt model reasonably matches the reference curve.

10 Conclusion

Our reduced numerical ribbon model appears as a fast, accurate and robust model for computing the static equilibrium of a thin elastic ribbon possibly subject to various constraints. As such, it offers an interesting alternative for computing the statics of perfectly inextensible surfaces, compared to a rod model, which fails to preserve inextensibility of the carried surface, or to a shell simulator, which becomes overly costly when the thickness vanishes. We also confirm that, in certain setups, physical narrow ribbons experience stretching deformation and we show that our numerical model is able to deal with these difficult cases. In the future, an interesting research path would be to investigate how to extend our model to deformations going beyond the Wunderlich constraint, that is involving kinks, sharp folds and even fracture, which naturally emerge in very thin surfaces like crumpled paper.

Acknowledgments

We would like to thank Basile Audoly and Gert van der Heijden, as well as Stéphanie Deboeuf, for sharing their preprints on the boundary layer treatment and on the spiral configuration, respectively. We are grateful to Victor Romero for providing us with laboratory experiments on the confined ribbon buckling problem, and to Basile Audoly for interesting discussions on the rolling conditions of the Möbius band. We also warmly thank Corrado Maurini and Kevin Korner for their help with the FEniCS-Shell code and the DER-Wunderlich code, respectively, as well as Octave Crespel and Lucas Frérot for their help in preparing the figures and movies with Blender. Finally, we would like to thank the anonymous reviewers for their constructive comments.

Appendices

A Force Curves in the Confined Ribbon Buckling Experiment

For the lineic and planar contact configurations only, we present here the numerical data for the total vertical compression force F as a function of the height H. As explained in [Roman and Pocheau 2002], for each Δ value, these curves collapse if the number n of folds is used to rescale both the horizontal and vertical axes: for example the data of Figure 19 is collapsed in the curve labelled $\Delta = 0.2$ in Figure 24.

We also present in Figure 25 a re-scaling of the axes for which the data of Figure 24 approximately follows a single master curve, valid for all Δ, given by Equation (31).

B The Shooting Approach

Variational approach. In this section, we show how to find equilibrium solutions of elastic ribbons in the Wunderlich model, in a shooting-based approach. We first show how to obtain differential equations and then how to solve the associated boundary value problem. We illustrate our approach with the Möbius configuration but it can be applied to other setups. We start with the Wunderlich deformation energy density in the absence of natural normal curvature $\check{\kappa}$

$$W_e = \frac{1}{2} D w \kappa^2 \left(1 + \eta^2\right)^2 \psi(w\eta'), \tag{33}$$

see Equation (6a) with $\check{\kappa} = 0$. We add the potential energy density associated with the ribbon weight $W_g = -\rho h w \mathbf{r} \cdot \mathbf{g}$, where $\mathbf{g}$ is the gravity vector, giving the direction and intensity of gravity. We seek to extremise (we include unstable equilibrium solutions)

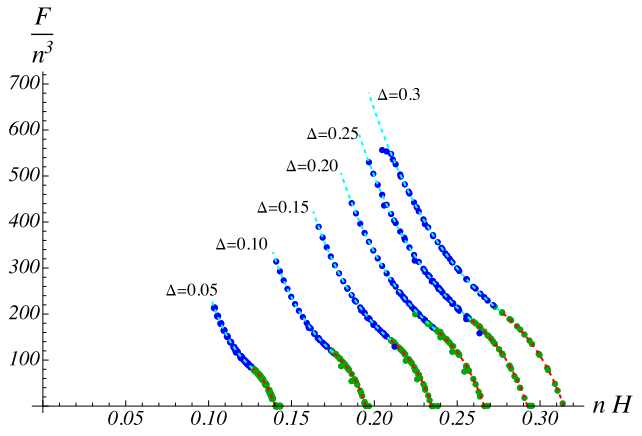

Fig. 24. Vertical force F on the cell with the scaling for both axes as introduced by Roman and Pocheau [1999]. Dotted lines correspond to analytical solutions of the planar Elastica with lineic and planar contact, and points correspond to numerical Merci data.

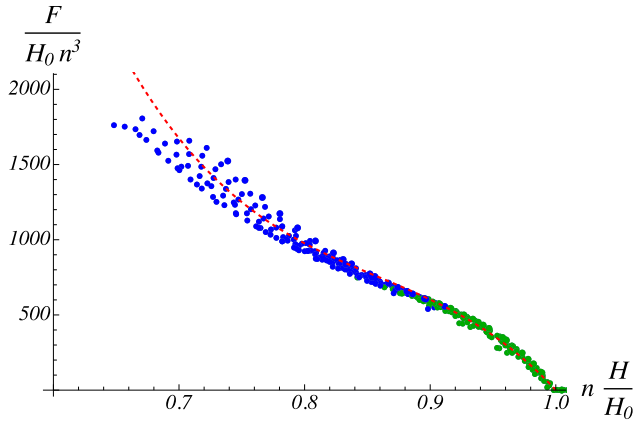

Fig. 25. Approximate collapse of the numerical data of Figure 24 for the vertical compression force F as a function of the height H of the cell, for $\Delta = 0.05, 0.1, 0.15, 0.20, 0.25, 0.3$. The number n of waves is such that $1 \le n \le 9$, and $H_0(\Delta)$ is the vertical height of the cell at first contact, see Equation (28). The red curve is given by (31).

the total energy $E_{\mathcal{W}} + E_G = \int_0^L (W_e + W_g)\, ds$ under several constraints. These constraints typically comprise boundary conditions on the position $\mathbf{r}$ and orientation of the material frame $(\mathbf{d}_1, \mathbf{d}_2, \mathbf{d}_3)$, which brings $\mathbf{r}$, $\mathbf{d}_1$, $\mathbf{d}_2$, $\mathbf{d}_3$ into the variational approach. Consequently, we have to consider additional relations (aka constraints) between these variables, namely

$$\mathbf{r}' = \mathbf{d}_3 \tag{34a}$$

$$\mathbf{d}_1 \cdot \mathbf{d}_2 = 0 \qquad \mathbf{d}_1 \cdot \mathbf{d}_3 = 0 \qquad \mathbf{d}_2 \cdot \mathbf{d}_3 = 0 \tag{34b}$$

$$\mathbf{d}_1 \cdot \mathbf{d}_1 = 1 \qquad \mathbf{d}_2 \cdot \mathbf{d}_2 = 1 \qquad \mathbf{d}_3 \cdot \mathbf{d}_3 = 1 \tag{34c}$$

$$\mathbf{d}_2' \cdot \mathbf{d}_3 = \kappa_1 \qquad \mathbf{d}_3' \cdot \mathbf{d}_1 = \kappa_2 \qquad \mathbf{d}_1' \cdot \mathbf{d}_2 = \kappa_3 \tag{34d}$$

Equations (34d) are equivalent to the Darboux equations (2) where we set $\kappa_1 = \kappa$, $\kappa_2 = 0$, $\kappa_3 = \eta\kappa$, see Section 4.1. For each of these constraints, we associate a Lagrange multiplier and work with the Lagrangian $\mathcal{L}(\kappa, \eta, \mathbf{r}, \mathbf{d}_1, \mathbf{d}_2, \mathbf{d}_3)$

$$\begin{aligned}\mathcal{L} =& W_e(\kappa,\eta) + W_g(\mathbf{r}) - \boldsymbol{\lambda}\cdot(\mathbf{d}_3 - \mathbf{r}') \\ &- \mu_1(\kappa - \mathbf{d}_2'\cdot\mathbf{d}_3) - \mu_2(0 - \mathbf{d}_3'\cdot\mathbf{d}_1) - \mu_3(\eta\kappa - \mathbf{d}_1'\cdot\mathbf{d}_2) \\ &- \nu_{12}\,\mathbf{d}_1\cdot\mathbf{d}_2 - \nu_{13}\,\mathbf{d}_1\cdot\mathbf{d}_3 - \nu_{23}\,\mathbf{d}_2\cdot\mathbf{d}_3 \\ &- \frac{1}{2}\epsilon_1(\mathbf{d}_1\cdot\mathbf{d}_1 - 1) - \frac{1}{2}\epsilon_2(\mathbf{d}_2\cdot\mathbf{d}_2 - 1) - \frac{1}{2}\epsilon_3(\mathbf{d}_3\cdot\mathbf{d}_3 - 1).\end{aligned} \tag{35}$$

Differential system of equilibrium equations. We work with nondimensionalised variables, that is in units where $D = 1$ and $L = 1$. This nondimensionalisation introduces the rescaled weight $\Gamma = \rho h g L^3/D$, see [Romero et al. 2021] for more details. We then compute the first variation of $\int_0^L \mathcal{L}\, ds$ and require that it vanishes for every variation of the variables $(\kappa, \eta, \mathbf{r}, \mathbf{d}_1, \mathbf{d}_2, \mathbf{d}_3)$, see [Elettro et al. 2017] for more details, which yields the differential system

$$\boldsymbol{\lambda}' = \Gamma\,\mathbf{g}, \tag{36a}$$

$$\mu_1' = \mu_2\,\eta\,\kappa + \boldsymbol{\lambda}\cdot\mathbf{d}_2, \tag{36b}$$

$$\mu_2' = \mu_3\,\kappa - \mu_1\,\eta\,\kappa - \boldsymbol{\lambda}\cdot\mathbf{d}_1, \tag{36c}$$

$$\mu_3' = -\mu_2\,\kappa, \tag{36d}$$

$$\mathbf{r}' = \mathbf{d}_3, \tag{36e}$$

$$\mathbf{d}_1' = \eta\,\kappa\,\mathbf{d}_2, \tag{36f}$$

$$\mathbf{d}_2' = \kappa\,\mathbf{d}_3 - \eta\,\kappa\,\mathbf{d}_1, \tag{36g}$$

$$\mathbf{d}_3' = -\kappa\,\mathbf{d}_2, \tag{36h}$$

$$0 = \kappa\,[1+\eta^2]^2\,\psi(w\eta') - \mu_1 - \mu_3\,\eta, \tag{36i}$$

$$\left(\kappa^2\,[1+\eta^2]^2\,\psi(w\eta')\right)' = 4\kappa^2\,\eta\,(1+\eta^2)\,\psi - 2\mu_3\,\kappa, \tag{36j}$$

Equation (36i) is used to isolate κ

$$\kappa = \frac{\mu_1 + \mu_3\,\eta}{[1+\eta^2]^2\,\psi(w\eta')}. \tag{37}$$

Equation (36j) is obtained after an integration by parts, which also yields the following natural boundary condition

$$\kappa^2\,[1+\eta^2]^2\,\psi(w\eta')\big|_{s=0,1} = 0, \tag{38}$$

which has to be fulfilled whenever $\eta(0)$ or $\eta(1)$ is not prescribed. We first factorise κ out of Equation (36j), and use (37) and its derivative to rewrite (36j) in the form

$$\begin{aligned}&2\eta(\mu_1+\mu_3\eta)w\eta'\frac{\dot\psi}{\psi} + (1+\eta^2)(w\boldsymbol{\lambda}\cdot\mathbf{d}_1 - \mu_3 w\eta')\frac{\dot\psi}{\psi} = \\ &-2\mu_1\eta - \mu_3\eta^2 + \mu_3 + \frac{\ddot\psi\psi - 2\dot\psi^2}{2\psi^2}(\mu_1+\mu_3\eta)(1+\eta^2)w^2\eta'' + \epsilon_r\eta'',\end{aligned} \tag{39}$$

where $(\,)' \equiv d/ds$ and $(\dot{}) \equiv d/d(w\eta')$. Please note that, in the same spirit as in [Moore and Healey 2019], we have added a regularisation term $\epsilon_r\,\eta''$. We use $0 < \epsilon_r \ll 1$ in the continuation procedure to go from the untwisted ($Lk = 0$) planar ring to the Möbius ($Lk = \frac{1}{2}$) configuration (equivalent to the procedure described in Algorithm 1). We then set $\epsilon_r = 0$ and vary the width w to obtain Möbius configurations for a wide range of width values (e.g., reaching values $w < 10^{-4}$).

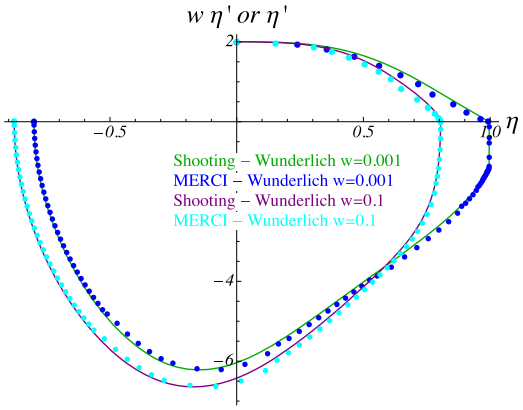

Fig. 26. Comparison between Merci and AUTO for the computation of the Möbius solution with the Wunderlich model.

With $\epsilon_r = 0$, we write (39) as two first-order differential equations, a form required by some ODE-based shooting solvers (e.g., AUTO [Doedel et al. 1991])

$$\eta' = d\eta, \tag{40a}$$

$$d\eta' = \frac{2}{(1+\eta^2)w^2}\left[Q_a\,(2\mu_1\eta + \mu_3\eta^2 - \mu_3) + 2\eta w\,d\eta\,P_b + (1+\eta^2)\,(w\,\boldsymbol{\lambda}\cdot\mathbf{d}_1 - \mu_3 w\,d\eta)\,Q_b\right], \tag{40b}$$

with

$$P_a = \frac{\psi^2}{\ddot{\psi}\,\psi - 2\dot{\psi}^2} \qquad P_b = \frac{\psi\,\dot{\psi}}{\ddot{\psi}\,\psi - 2\dot{\psi}^2}, \tag{41}$$

$$Q_a = \frac{P_a}{\mu_1 + \mu_3\,\eta} \qquad Q_b = \frac{P_b}{\mu_1 + \mu_3\,\eta}. \tag{42}$$

Please note that P_a and P_b remain bounded for $-2 \le w\eta' \le +2$ and that $P_a = 0 = P_b$ at singular points $w\eta' = \pm 2$. Nevertheless, as at singular points $\eta = 0 = \mu_1$, we have to ascertain the behaviour of Q_a and Q_b at these points.

Behaviour of Equations (39)–(40) at singular points. When the solution approaches the singularity $w\eta' = \pm 2$, Equations (40) simplifies to

$$\frac{d^2\eta}{d\sigma^2} = -2\,M\,\frac{1-\eta^2}{1+\eta^2}\left[Q_a + Q_b\,\frac{d\eta}{d\sigma}\right], \tag{43}$$

where $\sigma = s/w$ is the rapidly variable of the inner layer of the asymptotic expansion MAE introduced in [Audoly and van der Heijden 2022] in the case $w \ll 1$, and where the approximations $\mu_1(s) \simeq 0$, $\mu_3(s) \simeq M \simeq 19.7$, and $w\,\boldsymbol{\lambda}\cdot\mathbf{d}_1 \simeq 0$ have been used. Equation (43) can be integrated once

$$H = \frac{1}{2}\left(\frac{\eta}{1+\eta^2}\right)^2\left(\frac{1}{\psi} + \frac{\dot{\psi}}{\psi^2}\,\frac{d\eta}{d\sigma}\right). \tag{44}$$

The constant H is the Hamiltonian of the system, see [Starostin and van der Heijden 2015], and the inner layer of the Möbius solution corresponds to $H = 1/8$.

Using (44), we compute that as we approach the singular point, that is when $w\eta' = 2 - \epsilon$ with $\epsilon \to 0$, we have

$$\eta \sim \sqrt{\epsilon}\,\log(4/\epsilon) \to 0 \qquad \kappa \sim \sqrt{\epsilon} \to 0, \tag{45a}$$

$$\psi \sim \log(4/\epsilon) \qquad \dot{\psi} \sim 1/\epsilon, \tag{45b}$$

$$\ddot{\psi} \sim 1/\epsilon^2 \qquad W_e \sim \epsilon\log(4/\epsilon) \to 0, \tag{45c}$$

$$Q_a \sim \epsilon\,\sqrt{\epsilon} \to 0 \qquad Q_b \sim \frac{\sqrt{\epsilon}}{\log(4/\epsilon)} \to 0. \tag{45d}$$

These asymptotic behaviours show that, at the singular point, the differential system (40) behaves regularly and the elastic energy density vanishes.

Implementation in the AUTO code. The function $\psi(x)$ and its derivative suffers from catastrophic cancellation in the series for the two log terms when x is near 0. As in [Moore and Healey 2019], we replace $\psi(x)$ by ψ_{10}, its order 10 Taylor Expansion, whenever $|x| < 0.005$. When $0.005 < |x| < 2$, we use Equation (6b). Finally, when $2 \le |x|$ we use

$$\psi_{\text{AUTO}}(x) = \psi_{10} + \frac{1}{20}\,\frac{1}{4-x^2}. \tag{46}$$

This ad-hoc continuation of the Wunderlich function ψ is useful during the Newton-Raphson procedure in which the AUTO code tries to find a numerical solution to the boundary value problem. For some Newton steps, the code might wander in the forbidden region $2 \le |x|$ before converging inside the region $|x| < 2$. The present continuation (46) renders the $2 < |x|$ region available and hence prevents the Newton routine from crashing. It allowed us to decrease the width parameter w to values lower than 10^{-4} and verify the convergence of the numerical solution toward the asymptotic expansion (MAE) solution. Only at the singular point, the numerical value of $x = w\eta'$ was sometimes found to be $w\eta' \simeq 2.006$, slightly over 2.

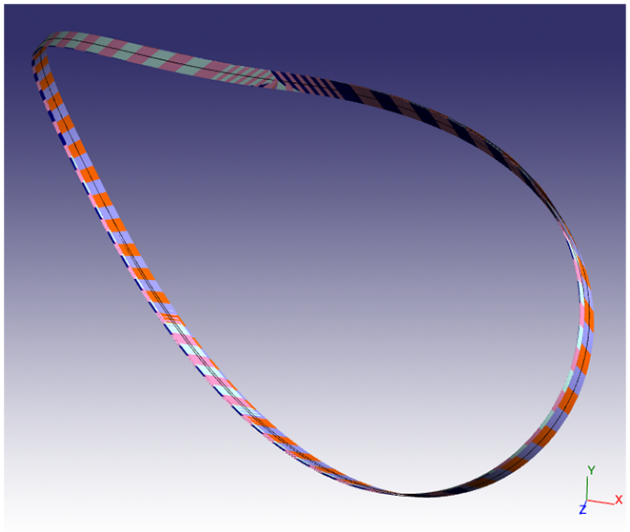

Fig. 27. Three ways to constrain the function $\eta(s)$ at $s = 0, L$. The overall shape is approximately the same. See Figure 28 for a zoom at the singular point.

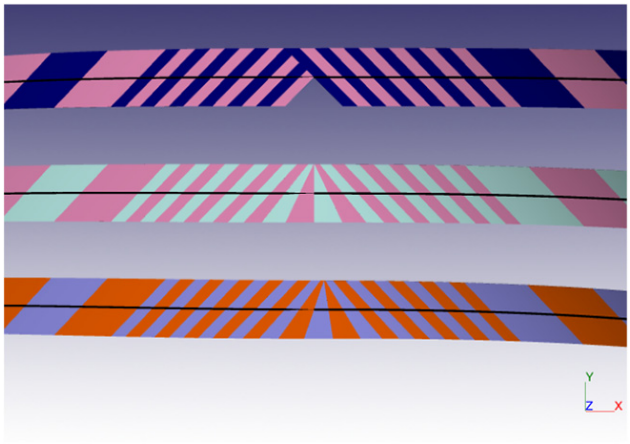

Fig. 28. Three ways to constrain the function $\eta(s)$ at $s = 0, L$. Zoom on the singular point. From bottom to top: $\eta(0) = -\eta(L)$, $\eta(0) = 0 = \eta(L)$, no constraint.

C Different Ways to Constrain $\eta(s)$

Here we compare different ways to constrain the function $\eta(s)$ at $s = 0, L$. We choose $s = 0$ to be the singular point, as in Section 7. Due to the Möbius construction, when crossing the $s = 0$ point, the directors $\mathbf{d}_1$ and $\mathbf{d}_2$ are rotated by an angle π around the director $\mathbf{d}_3$, that is we have $\mathbf{d}_{1,2}(0) = -\mathbf{d}_{1,2}(L)$. At $s = 0$, the moment and hence the Darboux vector $\mathbf{u}(s)$ are continuous. This implies that $\kappa(0) = -\kappa(L)$ but $\tau(0) = \tau(L)$, and hence $\eta(0) = -\eta(L)$ (NB: $\tau = \kappa\,\eta$). We run Merci with (i) the constraint $\eta(0) = -\eta(L)$, (ii) the constraint $\eta(0) = 0 = \eta(L)$, (iii) no constraint. We find that the shape is approximately the same in the three approaches, Figure 27, but that a closer look at the singular region shows that in order to have a continuous ribbon one should avoid the (i) approach, Figure 28.

D Universality of the Wunderlich Boundary Layer

Here we compute the equilibrium solution of the clamped-free ribbon in the Lateral Torsional Buckling (LTB) experiment. We use the Wunderlich model and enforce the $\eta(s = 0) = 0$ constraint in order to have a flat ribbon emerging from the clamp, see Section 9.3. At the buckling threshold, $\Gamma = 21.5$, the buckling mode in the Sadowsky model is known to have $\eta(0) = 1$ [Audoly and Neukirch 2021], and this property carries to post-buckled configurations, as illustrated in Figure 29. Therefore the enforcement of the constraint $\eta(0) = 0$ naturally creates a boundary layer near $s = 0$ in which the Wunderlich solution varies rapidly to (i) satisfy the condition $\eta(0) = 0$ and (ii) stay as near as possible to the Sadowsky solution. We define the extent of the boundary layer as $s \in (0, s^\star)$ where $s^\star$ is such that $\eta'(s^\star) = 0$, and we see that $s^\star = O(\frac{w}{L})$. For three distinct values of the the width w, in Figure 30 we show a parametric plot where the horizontal axis is $\eta(s)$ and the vertical axis is $w\,\eta'(s)$ for $s \in (0, s^\star)$ and $\eta'(s)$ for $s \in (s^\star, 1)$. We see that for all values of the width, the solution starts with $w\eta'(0) = 2$ which renders the logarithm term in Wunderlich energy singular, just as in the Möbius solution. Figure 30 also illustrates that, as w becomes smaller, the equilibrium solution tends toward the boundary layer solution computed in [Audoly and van der Heijden 2022] for $s \in (0, s^\star)$ and tends toward the Sadowsky solution for $s \in (s^\star, 1)$.

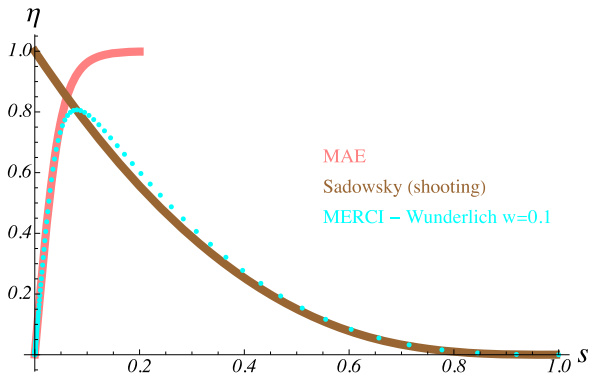

Fig. 29. (blue) Plot of $\eta(s)$ from Merci for the buckled LTB solution with Wunderlich model and constraint $\eta(0) = 0$, with $\Gamma = 30$ and $w = 0.1$. (pink) The boundary layer solution from [Audoly and van der Heijden 2022], and (brown) the Sadowsky solution.

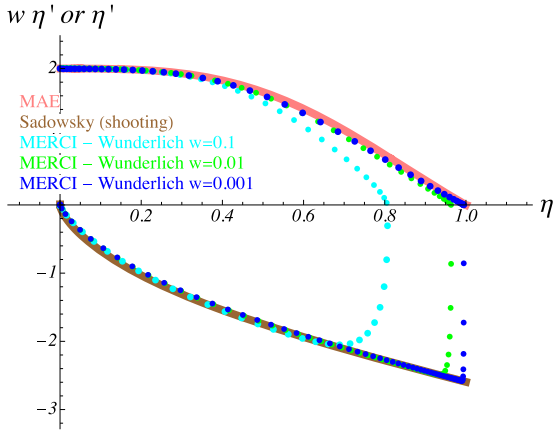

Fig. 30. Parametric plot of the buckled LTB solution with $\Gamma = 30$ and three values of the width w. Boundary (inner) layer in pink, Sadowsky (outer) solution in brown.

E Padé Approximants for the RibExt Energy

The function $\boldsymbol{\phi}(x)$ introduced in Equation (8b) contains the term

$$\frac{\cosh x - \cos x}{\sinh x + \sin x}, \tag{47}$$

for which we compute a $(4i - 3, 4i)$ Padé approximant, with i a strictly positive integer. The result is then injected in Equation (8b) and we obtain

$$i = 1: \quad \boldsymbol{\phi}_{\text{pade}}(x) = \frac{x^4}{180 + x^4}, \tag{48a}$$

$$i = 2: \quad \boldsymbol{\phi}_{\text{pade}}(x) = \frac{108108x^4 + 19x^8}{19459440 + 157860x^4 + 19x^8}, \tag{48b}$$

$$i = 3: \quad \boldsymbol{\phi}_{\text{pade}}(x) = \frac{ax^4 + bx^8 + 1822309x^{12}}{c + dx^4 + ex^8 + 1822309x^{12}}. \tag{48c}$$

$$a = 342728148082320\,, \quad b = 116476532172$$
$$c = 61691066654817600\,, \; d = 510577415908560$$
$$e = 140908262040$$

F LTB Bifurcation Curve for $\frac{w}{L} = 0.4$

We show here that for wide ribbons, $\frac{w}{L} = 0.4$, the agreement between the RibExt model and FEniCS-Shell data is not as good as in the narrow case, see Figure 31.

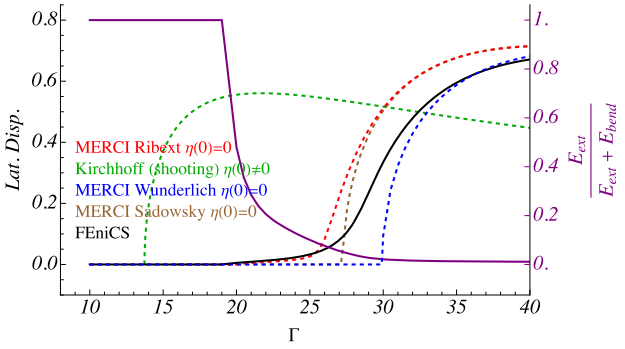

Fig. 31. Lateral Torsional Buckling bifurcation curve with $\nu = 0.35$, $\frac{w}{L} = 0.4$, and $\frac{h}{L} = 0.001$. Note that in the Merci code the constraints $\eta(0) = 0$ and $|w\eta'| \leq 2$ have been applied.

References

D. Arnold and F. Brezzi. 1997. Locking free finite element for shells. *Math. Comput.* 66, 217 (01 1997), 1–14. DOI: https://doi.org/10.1090/S0025-5718-97-00785-0

Basile Audoly and Sébastien Neukirch. 2021. A one-dimensional model for elastic ribbons: A little stretching makes a big difference. *Journal of the Mechanics and Physics of Solids* 153 (2021), 104457. DOI: https://doi.org/10.1016/j.jmps.2021.104457

Basile Audoly and Yves Pomeau. 2010. *Elasticity and Geometry: From Hair Curls to the Nonlinear Response of Shells.* Oxford University Press, Oxford.

Basile Audoly and G.H.M. van der Heijden. 2022. Analysis of cone-like singularities in twisted elastic ribbons. *Journal of the Mechanics and Physics of Solids* 171 (2022), 105131. DOI: 10.1016/j.jmps.2022.105131

D. Baraff and A. Witkin. 1998. Large steps in cloth simulation. In *Computer Graphics Proceedings (Proc. ACM SIGGRAPH'98).* ACM, Orlando, FL, 43–54. Retrieved from http://www.cs.cmu.edu/~baraff/papers/sig98.pdf

Sören Bartels and Peter Hornung. 2015. Bending paper and the Möbius strip. *Journal of Elasticity* 119, 1 (2015), 113–136.

M. Bergou, B. Audoly, E. Vouga, M. Wardetzky, and E. Grinspun. 2010. Discrete viscous threads. *ACM Transactions on Graphics* 29, 4, Article 116 (2010), 10 pages. DOI: https://doi.org/10.1145/1833349.1778853

M. Bergou, M. Wardetzky, S. Robinson, B. Audoly, and E. Grinspun. 2008. Discrete elastic rods. *ACM Transactions on Graphics (Proc. ACM SIGGRAPH'08)* 27, 3 (2008), 1–12. DOI: https://doi.org/10.1145/1360612.1360662

F. Bertails, B. Audoly, M.-P. Cani, B. Querleux, F. Leroy, and J.-L. Lévêque. 2006. Superhelices for predicting the dynamics of natural hair. *ACM Transactions on Graphics (Proc. ACM SIGGRAPH'06)* 25, 3 (2006), 1180–1187. DOI: https://doi.org/10.1145/1141911.1142012

Davide Bigoni. 2012. *Nonlinear Solids Mechanics.* Cambridge University Press, Cambridge, UK.

Pengbo Bo and Wenping Wang. 2007. Geodesic-controlled developable surfaces for modeling paper bending. *Computer Graphics Forum* 26, 3 (2007), 365–374. DOI: https://doi.org/10.1111/j.1467-8659.2007.01059.x

B. Boehm. 1981. *Software Engineering Economics.* Prentice-Hall, Englewood Cliffs, N.J..

Friedrich Bös, Max Wardetzky, Etienne Vouga, and Omer Gottesman. 2017. On the incompressibility of cylindrical origami patterns. *Journal of Mechanical Design* 139, 2 (2017), 021404. DOI: https://doi.org/10.1115/1.4034970

Richard Bradshaw, David Campbell, Mousa Gargari, Amir Mirmiran, and Patrick Tripeny. 2002. Special structures: Past, present, and future. *Journal of Structural Engineering* 128, 6 (2002), 691–709.

R. Bridson, S. Marino, and R. Fedkiw. 2003. Simulation of clothing with folds and wrinkles. In *ACM SIGGRAPH - EG Symposium on Computer Animation (SCA'03).* The Eurographics Association, Goslar, 28–36. Retrieved from http://www.cs.ubc.ca/~rbridson/docs/cloth2003.pdf

Michel Carignan, Ying Yang, Nadia Magnenat Thalmann, and Daniel Thalmann. 1992. Dressing animated synthetic actors with complex deformable clothes. *SIGGRAPH Comput. Graph.* 26, 2 (jul 1992), 99–104. DOI: https://doi.org/10.1145/142920.134017

R. Casati. 2015. *Quelques contributions à la modélisation numérique de structures élancées pour l'informatique graphique.* phdthesis. Université Grenoble Alpes. Retrieved from http://www.theses.fr/2015GREAM053/document

R. Casati and F. Bertails-Descoubes. 2013. Super space clothoids. *ACM Transactions on Graphics* 32, 4 (2013), 48. DOI: https://doi.org/10.1145/2461912.2461962

Herzl Chai. 2006. On the crush worthiness of a laterally confined bar under axial compression. *Transactions of the ASME* 73, 5 (2006), 834–841. DOI: 10.1115/1.2047595

Raphaël Charrondière, Florence Bertails-Descoubes, Sébastien Neukirch, and Victor Romero. 2020. Numerical modeling of inextensible elastic ribbons with curvature-based elements. *Computer Methods in Applied Mechanics and Engineering* 364 (2020), 112922. DOI: https://doi.org/10.1016/j.cma.2020.112922

H.-Y. Chen, A. Sastry, W. van Rees, and E. Vouga. 2018. Physical simulation of environmentally induced thin shell deformation. *ACM Trans. Graph.* 37, 4, Article 146 (July 2018), 13 pages. DOI: https://doi.org/10.1145/3197517.3201395

K.-J. Choi and H.-S. Ko. 2002. Stable but responsive cloth. *ACM Trans. Graph.* 21, 3 (July 2002), 604–611. DOI: https://doi.org/10.1145/566654.566624

Julien Chopin, Vincent Démery, and Benny Davidovitch. 2015. Roadmap to the morphological instabilities of a stretched twisted ribbon. *Journal of Elasticity* 119 (2015), 137–189. DOI: 10.1007/s10659-014-9498-

Stéphanie Deboeuf, Suzie Protière, and Eytan Katzav. 2024. Yin-yang spiraling transition of a confined buckled elastic sheet. *Physical Review Research* 6, 1 (2024), 013100. DOI: https://doi.org/10.1103/PhysRevResearch.6.013100

Philippe Decaudin, Dan Julius, Jamie Wither, Laurence Boissieux, Alla Sheffer, and Marie-Paule Cani. 2006. Virtual garments: A fully geometric approach for clothing design. *Computer Graphics Forum* 25, 3 (2006), 625–634. DOI: https://doi.org/10.1111/j.1467-8659.2006.00982.x

Marcelo A. Dias and Basile Audoly. 2014. A non-linear rod model for folded elastic strips. *Journal of the Mechanics and Physics of Solids* 62 (2014), 57–80. DOI: 10.1016/j.jmps.2013.08.012

Marcelo A. Dias and Basile Audoly. 2015. "Wunderlich, meet kirchhoff": A general and unified description of elastic ribbons and thin rods. *Journal of Elasticity* 119, 1 (2015), 49–66. DOI: https://doi.org/10.1007/s10659-014-9487-0

E. Dill. 1992. Kirchhoff's theory of rods. *Archive for History of Exact Sciences* 44, 1 (1992), 1–23.

Manfredo P Do Carmo. 2016. *Differential Geometry of Curves and Surfaces: Revised and Updated Second Edition.* Courier Dover Publications, Mineola, New York.

Eusebius Doedel, Herbert B. Keller, and Jean Pierre Kernevez. 1991. Numerical analysis and control of bifurcation problems (II): Bifurcation in infinite dimensions. *International Journal of Bifurcation and Chaos* 01, 4 (1991), 745–772.

G. Domokos, P. Holmes, and B. Royce. 1997. Constrained euler buckling. *Journal of Nonlinear Science* 7, 3 (1997), 281–314.

Levi H. Dudte, Etienne Vouga, Tomohiro Tachi, and L. Mahadevan. 2016. Programming curvature using origami tessellations. *Nature Materials* 15, 5 (2016), 583–588. DOI: https://doi.org/10.1038/nmat4540

Hervé Elettro, Paul Grandgeorge, and Sébastien Neukirch. 2017. Elastocapillary coiling of an elastic rod inside a drop. *Journal of Elasticity* 127, 2 (2017), 235–247.

E. English and R. Bridson. 2008. Animating developable surfaces using nonconforming elements. *ACM Transactions on Graphics (Proc. of SIGGRAPH'08)* 27, 3 (2008), 1–5. DOI: https://doi.org/10.1145/1360612.1360665

Roger Fosdick and Eliot Fried (Eds.). 2015. *The Mechanics of Ribbons and Moebius Bands.* Springer.

Lorenzo Freddi, Peter Hornung, Maria Giovanna Mora, and Roberto Paroni. 2016. A corrected sadowsky functional for inextensible elastic ribbons. *Journal of Elasticity* 123, 2 (2016), 125–136.

R. Goldenthal, D. Harmon, R. Fattal, M. Bercovier, and E. Grinspun. 2007. Efficient simulation of inextensible cloth. *ACM Transactions on Graphics (Proc. ACM SIGGRAPH'07)* 26, 3, Article 49 (2007), 7 pages. DOI: https://doi.org/10.1145/1275808.1276438

E. Grinspun, A. Hirani, M. Desbrun, and P. Schröder. 2003. Discrete shells. In *ACM SIGGRAPH - EG Symposium on Computer Animation (SCA'03).* The Eurographics Association, Goslar, Germany, 62–67. Retrieved from http://www.multires.caltech.edu/pubs/ds.pdf

M. Habera, J. S. Hale, A. Logg, C. Richardson, J. Ring, M. E. Rognes, N. Sime, and G. N. Wells. 2018. The Fenics Project. (2018). Retrieved from https://fenicsproject.org

S. Hadap. 2006. Oriented strands - Dynamics of stiff multi-body system. In *ACM SIGGRAPH - EG Symposium on Computer Animation (SCA'06).* Eurographics Association, Vienna, Austria, 91–100.

Christian Hafner and Bernd Bickel. 2021. The design space of plane elastic curves. *ACM Transactions on Graphics (TOG)* 40, 4 (2021), 1–20. DOI: https://doi.org/10.1145/3450626.3459800

Jack S. Hale, Matteo Brunetti, Stéphane P. A. Bordas, and Corrado Maurini. 2018. Simple and extensible plate and shell finite element models through automatic code generation tools. *Computers & Structures* 209 (2018), 163–181. DOI: 10.1016/j.compstruc.2018.08.001

M. Hauth, O. Etzmuss, and W. Strasser. 2003. Analysis of numerical methods for the simulation of deformable models. *The Visual Computer* 19 (2003), 581–600. DOI: 10.1007/s00371-003-0206-2

Denis F. Hinz and Eliot Fried. 2015. Translation of michael sadowsky's paper "the differential equations of the Möbius band". *Journal of Elasticity* 119, 1 (2015), 19–22.

Weicheng Huang, Chao Ma, Qiang Chen, and Longhui Qin. 2022. A discrete differential geometry-based numerical framework for extensible ribbons. *International Journal of Solids and Structures* 248 (2022), 111619. DOI: https://doi.org/10.1016/j.ijsolstr.2022.111619

Weicheng Huang, Yunbo Wang, Xuanhe Li, and Mohammad K. Jawed. 2020. Shear induced supercritical pitchfork bifurcation of pre-buckled bands, from narrow strips to wide plates. *Journal of the Mechanics and Physics of Solids* 145 (2020), 104168. DOI: https://doi.org/10.1016/j.jmps.2020.104168

Victor Ceballos Inza, Florian Rist, Johannes Wallner, and Helmut Pottmann. 2023. Developable quad meshes and contact element nets. *Transactions on Graphics (TOG)* 42, 6 (2023), 183. DOI: https://doi.org/10.1145/

David Jourdan, Mélina Skouras, Etienne Vouga, and Adrien Bousseau. 2022. Computational design of self-actuated surfaces by printing plastic ribbons on stretched fabric. *Computer Graphics Forum* 41, 2 (April 2022), 1–14. Retrieved from https://hal.inria.fr/hal-03588434

Martin Kilian, Simon Flöry, Zhonggui Chen, Niloy J. Mitra, Alla Sheffer, and Helmut Pottmann. 2008. Curved folding. *ACM Trans. Graph.* 27, 3 (aug 2008), 1–9. DOI: https://doi.org/10.1145/1360612.1360674

Kevin Korner, Basile Audoly, and Kaushik Bhattacharya. 2021. Simple deformation measures for discrete elastic rods and ribbons. *Proceedings of the Royal Society A* 477, 2256 (2021), 20210561.

Arun Kumar, Poornakanta Handral, Darshan Bhandari, and Ramsharan Rangarajan. 2021. More views of a one-sided surface: Mechanical models and stereo vision techniques for Möbius strips. *Proceedings of the Royal Society A* 477, 2250 (2021), 20210076. DOI: 10.1098/rspa.2021.0076

A. Kumar, P. Handral, C. S. Darshan Bhandari, A. Karmakarn, and R. Rangarajan. 2020. An investigation of models for elastic ribbons: Simulations & experiments. *Journal of the Mechanics and Physics of Solids* 143 (2020), 104070.

Claire Lestringant and Dennis M. Kochmann. 2020. Modeling of flexible beam networks and morphing structures by geometrically exact discrete beams. *Journal of Applied Mechanics* 87, 8 (05 2020), 081006. DOI: https://doi.org/10.1115/1.4046895

Yang Liu, Helmut Pottmann, Johannes Wallner, Yong-Liang Yang, and Wenping Wang. 2006. Geometric modeling with conical meshes and developable surfaces. *ACM Trans. Graph.* 25, 3 (jul 2006), 681–689. DOI: https://doi.org/10.1145/1141911.1141941

A. E. H. Love. 1944. *A Treatise on the Mathematical Theory of Elasticity* (4th ed.). Dover Publications, New York.

David G. Luenberger. 1973. *Introduction to Linear and Nonlinear Programming* (3rd ed.). Addison-Wesley, New York.

A. I. Lurie. 2005. *Theory of Elasticity*. Springer, Berlin.

L. Mahadevan and J. B. Keller. 1993. The shape of a Möbius band. *Proc. R. Soc. Lond. A* 440, 1908 (1993), 149–162. DOI: 10.1098/rspa.1993.0009

A. G. M. Michell. 1899. Elastic stability of long beams under transverse forces. *The London, Edinburgh, and Dublin Philosophical Magazine and Journal of Science* 48, 292 (1899), 298–309.

J. T. Miller, T. Su, J. Pabon, N. Wicks, K. Bertoldi, and P.M. Reis. 2015. Buckling of a thin elastic rod inside a horizontal cylindrical constraint. *Extreme Mechanics Letters* 3 (2015), 36–44. DOI: 10.1016/j.eml.2015.03.002

Alexander Moore and Timothy Healey. 2019. Computation of elastic equilibria of complete Möbius bands and their stability. *Mathematics and Mechanics of Solids* 24, 4 (2019), 939–967. DOI: https://doi.org/10.1177/1081286518761789

P. M. Naghdi. 1963. Foundations of elastic shell theory. In *Progress in Solid Mechanics*, I. N. Sneddon and R. Hill (Eds.). Vol. 4. North-Holland, Amsterdam, 1–90.

R. Narain, A. Samii, and J. O'Brien. 2012. Adaptive anisotropic remeshing for cloth simulation. *ACM Trans. Graph.* 31, 6, Article 152 (Nov. 2012), 10 pages. DOI: https://doi.org/10.1145/2366145.2366171

Sébastien Neukirch and Basile Audoly. 2021. A convenient formulation of Sadowsky's model for elastic ribbons. *Proc. R. Soc. A* 477, 2255 (2021), 20210548. DOI: 10.1098/rspa.2021.0548

Jorge Nocedal, Andreas Wächter, and Richard A. Waltz. 2009. Adaptive barrier update strategies for nonlinear interior methods. *SIAM Journal on Optimization* 19, 4 (2009), 1674–1693. DOI: https://doi.org/10.1137/060649513

D. Pai. 2002. Strands: Interactive simulation of thin solids using cosserat models. *Computer Graphics Forum (Proc. Eurographics'02)* 21, 3 (2002), 347–352.

Zherong Pan, Jin Huang, and Hujun Bao. 2016. Modelling developable ribbons using ruling bending coordinates. *Computing Research Repository* abs/1603.04060 (2016), 1–9. arXiv:1603.04060. Retrieved from https://arxiv.org/abs/1603.04060

H. Pham. 2006. *System Software Reliability*. Springer, London.

Nico Pietroni, Corentin Dumery, Raphael Falque, Mark Liu, Teresa Vidal-Calleja, and Olga Sorkine-Hornung. 2022. Computational pattern making from 3D garment models. *ACM Transactions on Graphics* 41, 4 (2022), 157:1–14.

A. Pocheau and B. Roman. 2004. Uniqueness of solutions for constrained Elastica. *Physica D: Nonlinear Phenomena* 192, 3-4 (2004), 161–186.

Helmut Pottmann and Gerald Farin. 1995. Developable rational Bézier and B-spline surfaces. *Computer Aided Geometric Design* 12, 5 (1995), 513–531. DOI: https://doi.org/10.1016/0167-8396(94)00031-M

Xavier Provot. 1995. Deformation constraints in a mass-spring model to describe rigid cloth behaviour. In *Proceedings of Graphics Interface'95 (GI'95)*. Canadian Human-Computer Communications Society, Toronto, Ontario, Canada, 147–154. Retrieved from http://graphicsinterface.org/wp-content/uploads/gi1995-17.pdf

Michael Rabinovich, Tim Hoffmann, and Olga Sorkine-Hornung. 2018a. Discrete geodesic nets for modeling developable surfaces. *ACM Trans. Graph.* 37, 2, Article 16 (feb 2018), 17 pages. DOI: https://doi.org/10.1145/3180494

Michael Rabinovich, Tim Hoffmann, and Olga Sorkine-Hornung. 2018b. The shape space of discrete orthogonal geodesic nets. *ACM Transactions on Graphics (proceedings of ACM SIGGRAPH ASIA)* 37, 6, Article 228 (2018), 17 pages. DOI: https://doi.org/10.1145/3272127.3275088

E. Reissner. 1989. Lateral buckling of beams. *Computers & Structures* 33, 5 (1989), 1289–1306.

Yingying Ren, Julian Panetta, Tian Chen, Florin Isvoranu, Samuel Poincloux, Christopher Brandt, Alison Martin, and Mark Pauly. 2021. 3D weaving with curved ribbons. *ACM Trans. Graph.* 40, 4, Article 127 (July 2021), 15 pages. DOI: https://doi.org/10.1145/3450626.3459788

B. Roman and A. Pocheau. 1999. Buckling cascade of thin plates: Forms, constraints and similarity. *Europhysics Letters (EPL)* 46, 5 (1999), 602–608. DOI: https://doi.org/10.1209/epl/i1999-00306-3

B. Roman and A. Pocheau. 2002. Postbuckling of bilaterally constrained rectangular thin plates. *Journal of the Mechanics and Physics of Solids* 50 (2002), 2379–2401. DOI: 10.1016/S0022-5096(02)00028-5

Victor Romero, Mickaël Ly, Abdullah-Haroon Rasheed, Raphaël Charrondière, Arnaud Lazarus, Sébastien Neukirch, and Florence Bertails-Descoubes. 2021. Physical validation of simulators in Computer Graphics: A new framework dedicated to slender elastic structures and frictional contact. *ACM Transactions on Graphics* 40, 4 (2021), 1–18. Retrieved from https://hal.inria.fr/hal-03217459

Michael Sadowsky. 1929. Die differentialgleichungen des MÖBIUSschen bandes. *Jahresbericht der Deutschen Mathematiker-Vereinigung* 39 (1929), 49–51.

Tomohiko G. Sano and Hirofumi Wada. 2018. Snap-buckling in asymmetrically constrained elastic strips. *Phys. Rev. E* 97, 1 (Jan. 2018), 013002. DOI: https://doi.org/10.1103/PhysRevE.97.013002

Tomohiko G. Sano and Hirofumi Wada. 2019. Twist-induced snapping in a bent elastic rod and ribbon. *Phys. Rev. Lett.* 122, 11 (2019), 114301. DOI: 10.1103/PhysRevLett.122.114301

Camille Schreck, Damien Rohmer, Stefanie Hahmann, Marie-Paule Cani, Shuo Jin, Charlie C. L. Wang, and Jean-Francis Bloch. 2015. Non-smooth developable geometry for interactively animating paper crumpling. *ACM Transactions on Graphics* 35, 1 (Dec. 2015), 18. DOI: https://doi.org/10.1145/2829948

G. E. Schwarz. 1990. The dark side of the moebius strip. *The American Mathematical Monthly* 97, 10 (1990), 890–897.

Zhongwei Shen, Jin Huang, Wei Chen, and Hujun Bao. 2015. Geometrically exact simulation of inextensible ribbon. *Computer Graphics Forum* 34, 7 (2015), 145–154. DOI: https://doi.org/10.1111/cgf.12753

R. T. Shield. 1992. Bending of a beam or wide strip. *Quarterly Journal of Mechanics and Applied Mathematics* 45, 4 (1992), 567–573.

Madlaina Signer, Alexandra Ion, and Olga Sorkine-Hornung. 2021. Developable metamaterials: Mass-fabricable metamaterials by laser-cutting elastic structures. In *CHI'21: Proceedings of the 2021 CHI Conference on Human Factors in Computing Systems*. Association for Computing Machinery, New York, NY, 1–13. DOI: https://doi.org/10.1145/3411764.3445666

Justin Solomon, Etienne Vouga, Max Wardetzky, and Eitan Grinspun. 2012. Flexible developable surfaces. *Comput. Graph. Forum* 31, 5 (aug 2012), 1567–1576. DOI: https://doi.org/10.1111/j.1467-8659.2012.03162.x

Valentin Sonneville and Olivier Brüls. 2014. A formulation on the special euclidean group for dynamic analysis of multibody systems. *Journal of Computational and Nonlinear Dynamics* 9, 4 (2014), 041002. DOI: 10.1115/1.4026569

J. Spillmann and M. Teschner. 2007. CoRdE: Cosserat rod elements for the dynamic simulation of one-dimensional elastic objects. In *ACM SIGGRAPH - EG Symposium on Computer Animation (SCA'07)*. ACM-EG SCA, San Diego, CA, 63–72.

E. L. Starostin and G. H. M. van der Heijden. 2007. The shape of a Möbius strip. *Nature Materials* 6, 8 (2007), 563. DOI: https://doi.org/10.1038/nmat1929

E. L. Starostin and G. H. M. van der Heijden. 2015. Equilibrium shapes with stress localisation for inextensible elastic Möbius and other strips. *Journal of Elasticity* 119, 1 (2015), 67–112.

Chengcheng Tang, Pengbo Bo, Johannes Wallner, and Helmut Pottmann. 2016. Interactive design of developable surfaces. *ACM Trans. Graph.* 35, 2, Article 12 (jan 2016), 12 pages. DOI: https://doi.org/10.1145/2832906

Demetri Terzopoulos, John Platt, Alan Barr, and Kurt Fleischer. 1987. Elastically deformable models. *ACM Transactions on Graphics* 21, 4 (1987), 205–214. DOI: https://doi.org/10.1145/37402.37427

Bernhard Thomaszewski, Simon Pabst, and Wolfgang Straßer. 2009. Continuum-based strain limiting. *Computer Graphics Forum* 28, 2 (2009), 569–576. DOI: https://doi.org/10.1111/j.1467-8659.2009.01397.x

J. M. T. Thompson, M. Silveira, G. H. M. van der Heijden, and M. Wiercigroch. 2012. Helical post-buckling of a rod in a cylinder: With applications to drill-strings. *Proceedings of the Royal Society A: Mathematical, Physical and Engineering Science* 468, 2142 (2012), 1591–1614.

Russell E. Todres. 2015. Translation of W. Wunderlich's "On a developable Möbius band". *Journal of Elasticity* 119, 1 (2015), 23–34.

Petia Svetomirova Tzokova. 2020. *Confined wrinkling of thin elastic rods, sheets and cones*. Ph.D. Dissertation. University of Cambridge. Retrieved from www.repository.cam.ac.uk/handle/1810/310886

J. Vekhter, J. Zhuo, L. Fandino, Q. Huang, and E. Vouga. 2019. Weaving geodesic foliations. *ACM Trans. Graph.* 38, 4, Article 34 (July 2019), 22 pages. DOI: https://doi.org/10.1145/3306346.3323043

Andreas Wächter and Lorenz T. Biegler. 2006. On the implementation of an interior-point filter line-search algorithm for large-scale nonlinear programming. *Mathematical Programming* 106, 1 (2006), 25–57. DOI: https://doi.org/10.1007/s10107-004-0559-y

Thomas Wolf, Victor Cornillère, and Olga Sorkine-Hornung. 2021. Physically-based book simulation with freeform developable surfaces. *Computer Graphics Forum (proceedings of EUROGRAPHICS 2021)* 40, 2 (2021), 449–460. DOI: https://doi.org/10.1111/cgf.142646

W. Wunderlich. 1962. Über ein abwickelbares Möbiusband. *Monatshefte für Mathematik* 66, 3 (1962), 276–289. DOI: https://doi.org/10.1007/BF01299052

Tian Yu, Ignacio Andrade-Silva, Marcelo A. Dias, and J.A. Hanna. 2021. Cutting holes in bistable folds. *Mechanics Research Communications* 124 (2021), 103700. DOI: 10.1016/j.mechrescom.2021.103700

Received 28 June 2023; revised 13 March 2024; accepted 1 May 2024